Title:

Lactate Accelerates Mouse ES Cell Differentiation Towards the XEN Lineage

Running Title:

Lactate Potentiates XEN induction *in vitro*

Authors/Affiliations:

Mohamed I. Gatie[1,2*], Tyler T. Cooper[3], Gilles A. Lajoie[3,4], Gregory M. Kelly[1,2,4,5,6]

Author List Footnotes:

[1] Department of Biology, Western University, London, ON, Canada

[2] Collaborative Specialization in Developmental Biology, Western University, London, ON, Canada

[3] Department of Biochemistry, Don Rix Protein Identification Facility, Lawson Health Research Institute, Western University, London, Ontario, Canada

[4] Lawson Health Research Institute, Western University, London, ON, Canada

[5] Department of Physiology and Pharmacology, Western University, London, ON, Canada

[6] Child Health Research Institute, London, ON, Canada

Contact information:

[*]Correspondence: mgatie@uwo.ca

Summary:

Metabolism plays a crucial role for cell survival and function; however, recent evidence has implicated it in regulating embryonic development. The inner cell mass undergoes orchestrated cellular divisions resulting in the formation of embryonic stem cells and extraembryonic endoderm (XEN) cells. Concomitantly, changes in the metabolic profile occurs during development and are well-documented in the embryonic lineages. However, a comprehensive multi-omics analysis of these features in XEN cells remains lacking. We observed that feeder-free XEN cells exhibited high sensitivity to glycolytic inhibition in addition to maintaining elevated intra- and extracellular lactate levels. XEN cells maintain high lactate levels by increased LDHA activity and re-routing pyruvate away from the mitochondria. Importantly, exogenous lactate supplementation or promoting intracellular lactate accumulation enhances XEN differentiation *in vitro*. Our results highlight how lactate contributes to XEN differentiation in the mammalian embryo and may serve to enhance reprogramming efficiency of cells used for regenerative medicine.

Highlights:

- Feeder-free XEN cells exhibit high sensitivity to glycolytic inhibition
- Distinct transcriptomic, proteomic and metabolomic profile exists between feeder-free ES and XEN cells
- Elevated intracellular and extracellular lactate is observed in feeder-free XEN cells
- Lactate enhances feeder-free XEN differentiation *in vitro*

Keywords:

Embryonic stem cells

Extraembryonic endoderm cells

Pluripotency

Differentiation

Glycolysis

Oxidative Phosphorylation

Metabolites

Lactate

47 # Introduction

48 The early mammalian blastocyst is comprised of two distinct layers: the inner cell
49 mass (ICM) and trophectoderm. The ICM houses embryonic stem (ES) cells and primitive
50 endoderm cells, and the latter differentiate into parietal and visceral endoderm cells.
51 Collectively primitive, parietal and visceral endoderm cells make up the extraembryonic
52 endoderm (XEN) lineage. Various ES cells have been cultured at different developmental
53 time-points (Evans and Kaufman, 1981), each requiring specific conditions. For instance,
54 preimplantation ICM cells represent a “naïve” state and can be artificially maintained
55 under LIF and serum/BMP (Nichols et al., 1990) or defined conditions of LIF-2i in N2B27
56 media where dual inhibition of glycogen synthase kinase 3 and mitogen-activated protein
57 kinase pathways maintain pluripotency (Ying et al., 2008). However, the post-implantation
58 or “primed” epiblast stem cells, which are poised to give rise to the embryo proper, require
59 Activin A and FGF2 in culture (Brons et al., 2007). In addition to differences in culture
60 conditions, both naïve and primed states differ in their expression profile of pluripotency
61 core genes, DNA methylation, histone modification status, clonogenicity and chimera
62 contribution (Davidson et al., 2015). XEN cells, which contribute to both embryonic and
63 extraembryonic endoderm tissue (Nowotschin et al., 2019), have been derived by
64 isolation from blastocyst (Niakan et al., 2013), differentiated using exogenous factors
65 (Anderson et al., 2017; Cho et al., 2012; Soprano et al., 2007), reprogrammed from
66 fibroblast cells (He et al., 2020; Parenti et al., 2016), or form after the overexpression of
67 *Gata4/6* (Fujikura et al., 2002; Shimosato et al., 2007) or *Sox17* (McDonald et al., 2014).
68 In addition, evidence indicates that the metabolic state between embryonic and

69 extraembryonic lineages differs, suggesting that metabolism may be sufficient to
70 influence lineage commitment.

71 Naïve ES cells exhibit a bivalent metabolic profile, relying on glycolysis and
72 oxidative phosphorylation (OXPHOS) to generate energy, while epiblast stem cells are
73 exclusively glycolytic, despite displaying a mature mitochondrial ultrastructure (Zhou et
74 al., 2012). Although the majority of studies have focused on naïve and primed ES cells,
75 recent reports on extraembryonic cells show they are reliant on OXPHOS metabolism
76 (Choi et al., 2020), with a similar mitochondrial ultrastructure to epiblast stem cells (Seo
77 et al., 2020; Zhou et al., 2012). However, details on the comprehensive intracellular profile
78 of metabolites and their role during differentiation remains unknown.

79 Small metabolites have garnered attention with their role in maintaining
80 pluripotency, promoting differentiation and enhancing reprogramming efficiency of
81 induced pluripotent stem cells (Mathieu and Ruohola-Baker, 2017; Tsogtbaatar et al.,
82 2020; Zhang et al., 2012). These small compounds play integral roles in energy
83 production and epigenetic modifications. For instance, short-chain and saturated fatty
84 acids can modulate histone deacetylases and the epigenetic landscape and thus are
85 implicated in enhancing the efficiency of stem cell differentiation (Mali et al., 2010; Yanes
86 et al., 2010). Also, the depletion of threonine or loss of threonine dehydrogenase (TDH)
87 impacts stemness (Wang et al., 2009), while supplementation of L-threonine maintains
88 pluripotency (Ryu and Han, 2011). Therefore, naturally occurring metabolites play an
89 important role in regulating pluripotency and differentiation of stem cells by modulating
90 the metabolic and epigenetic landscape.

91 In this report we used a multi-omics approach to identify metabolic changes in cells
92 of the ICM and have further characterized the metabolic pathways involved in regulating
93 XEN lineage commitment. Overall, we observed a significant reduction in the survival of
94 feeder-free XEN cells following glycolytic inhibition. Transcriptomic and proteomic
95 profiling implicate lactate metabolism in regulating the differentiation towards the XEN
96 lineage. Strikingly, lactate was enriched intra- and extracellularly in feeder-free XEN cells,
97 and promoting intracellular lactate accumulation or supplementing with exogenous L-
98 lactate enhanced XEN induction. Together our results elucidate an unacknowledged role
99 for lactate in cell differentiation and fate commitment in the early mammalian embryo.

100 # Results

101 **ES cells are less sensitive to glycolytic inhibition than XEN cells**

102 A recent report characterized the metabolic profile of XEN cells as reliant on
103 OXPHOS metabolism (Choi et al., 2020). Albeit informative, this study derived and
104 maintained XEN cells on inactivated mouse embryonic fibroblasts, which are oxidative in
105 nature (Folmes et al., 2011) and are known to reduce the reliance of pluripotent stem
106 cells on glycolysis (Gu et al., 2016). To address if culturing methods influence the
107 metabolic profiles, ES-E14TG2a embryonic stem cells (ES cells) and extraembryonic
108 endoderm cells (XEN cells) (Kunath et al., 2005) were cultured under feeder-free
109 conditions in media containing 50mM 2-Deoxy-D-glucose (2-DG; glycolysis inhibitor) or
110 2.5μM oligomycin (OXPHOS inhibitor), and results were compared with cells grown under
111 control conditions (Figure 1). ES cells displayed domed-homogenous colonies while XEN
112 cells were single-celled, with two distinct morphologies present in culture, spindle-like or
113 round and refractile in nature (Figure 1A, Figure S1A).

114 ES colony shape appeared to be insensitive to 2-DG and oligomycin treatment;
115 however, XEN cells lost their distinct morphologies, particularly in the 2-DG treatment and
116 adopted a spindle-like morphology, indicative of cell stress (Figure 1A). In contrast to a
117 previous report (Choi et al., 2020), XEN cells were more sensitive to glycolytic inhibition
118 (5.87% ± 1.82) than OXPHOS inhibition with oligomycin (41.3% ± 7.30; $P < 0.01$; Figure
119 1B). Since ES cells are metabolically bivalent (Zhou et al., 2012), the significant reduction
120 in cell viability under both treatments was expected ($P < 0.01$) and not significant between
121 the two treatments (2-DG: 45.3% ± 8.84 *versus* oligomycin: 62.7% ± 5.24; Figure 1B).
122 Despite this reduction in cell viability, no change in relative total ATP levels was observed

123 between the two populations and treatments (Figure 1C). Collectively, our findings
124 support the notion that feeder-free XEN cells are more sensitive to glycolytic inhibition
125 than feeder-free ES cells.

126 **Intracellular metabolomic profiling of ICM cells**

127 Since feeder-free ES and XEN cells responded differently to metabolic inhibitors,
128 we exploited the feeder-free system to identify changes in intracellular metabolites
129 between the two populations. For metabolite identification, untargeted metabolomics was
130 used to measure the relative levels of intracellular metabolites (Figure 2). We identified
131 142 intracellular metabolites of which 18 were significantly enriched in ES cells and 68 in
132 XEN cells (Table 1; Figure 2A). Next, targeted metabolomics was performed to quantify
133 the levels of amino acids (Figure 2B) and metabolites involved in glycolysis and the
134 tricarboxylic acid (TCA) cycle (Figure 2C). Several amino acids were significantly
135 enriched in XEN cells, including proline, serine and threonine, which are reported to play
136 a role in pluripotency and differentiation (Baksh et al., 2020; Comes et al., 2013; Ryu and
137 Han, 2011; Wang et al., 2009). While most metabolites involved in glycolysis and TCA
138 cycle were not statistically significant, intracellular lactate and 2-hydroxyglutarate were
139 significantly higher in XEN cells when compared with ES cells ($P < 0.05$; Figure 2C).
140 Together, our data indicate that XEN cells exhibit a unique metabolite profile that is
141 distinct from the ES population.

142 **Transcriptomic and proteomic analysis showcases the importance of metabolic**
143 **pathways during embryonic development**

144 Bulk transcriptomic and proteomic analyses were performed on ES and XEN cells
145 in order to compare global gene expression and protein abundance patterns and assign

146 molecular pathway(s) to the metabolite profiles. Results revealed 2742 genes (Figure 3A)
147 and 165 proteins (Figure 3B) significantly upregulated in the ES population. In contrast,
148 1716 genes (Figure 3A) and 298 proteins (Figure 3B) were significantly upregulated in
149 XEN cells. As expected, markers of pluripotency including *Nanog*, *Sox2*, OCT4 and
150 ESRRB were enriched in the ES population, while XEN markers such as *Gata4/6*,
151 *Sox7/17*, *Dab2*, and PDGFRA were significantly enriched in XEN cells (Figure 3A, B).
152 Differentially expressed genes and proteins enriched in either ES or XEN cells were
153 selected and analyzed by gene ontology to classify targets based on their biological
154 process (Figure S2A-D), cellular compartment (Figure S2E-H) and molecular process
155 (Figure S2I-L). As expected, targets from ES cells were enriched for biological processes
156 associated with multicellular organism development and regulation of transcription
157 (Figure S3A, B). Conversely, XEN cells terms were associated with various signaling
158 pathways, endodermal development and extracellular matrix organization (Figure S3C,
159 D).

160 Kyoto Encyclopedia of Genes and Genomes (KEGG) enrichment analysis was
161 also performed on genes and proteins to identify biological pathways specific to each
162 population (Figure 3C-G). XEN cells expressed targets primarily involved in proteoglycan
163 metabolism and endoplasmic reticulum processing (Figure 3F, G, S3G, H), as reported
164 previously (Choi et al., 2020). However, metabolism of xenobiotics by cytochrome P450
165 and glucose/pyruvate metabolism were enriched in the ES population and represent two
166 common KEGG pathways between the RNAseq and MS datasets (Figure 3C, D).
167 Interestingly, three targets that were highly enriched in both datasets and linked to
168 glucose metabolism were aldehyde dehydrogenase 1 family member B1 (ALDH1B1),

169 phosphoenolpyruvate carboxykinase 2 (PCK2) and lactate dehydrogenase B (LDHB,
170 Figure 3E). Together, this data would suggest that these targets and their metabolites
171 play a role in either maintaining pluripotency or in the differentiation towards the XEN
172 lineage.

173 **Enzymes involved in lactate homeostasis are upregulated in feeder-free XEN cells**

174 Pyruvate is converted into lactate by the activity of LDHA and converted back by
175 LDHB; since the latter was enriched in the ES population (Figure 3A-E), and lactate was
176 enriched in XEN cells intracellularly (Figure 2C), we sought to further investigate the
177 levels of enzymes involved in lactate metabolism. qRT-PCR results showed significantly
178 higher *Ldha*/*Ldhb* expression in XEN cells compared with ES cells ($P < 0.01$, Figure 4A),
179 and this was confirmed at the protein level using immunoblot analysis (Figure 4B).
180 Extracellular lactate levels were also measured, and results showed significantly higher
181 levels in XEN cells ($P < 0.05$, Figure 4C). Furthermore, the expression of the lactate
182 transporter *Mct1* (Figure 4D), but not *Mct4* (Figure 4E), was significantly upregulated in
183 XEN cells ($P < 0.0001$) and is a prime candidate linked to these high extracellular lactate
184 levels. Pyruvate can also be oxidized in the mitochondria by the pyruvate dehydrogenase
185 complex (PDC) to generate acetyl-CoA. This conversion is dependent on the activity of
186 the PDC, which is negatively regulated by phosphorylation of the E1α subunit by
187 members of the pyruvate dehydrogenase kinase (PDK) family. Expression analysis
188 shows that *Pdk1, 2* and *4,* but not *Pdk3,* were significantly downregulated in XEN cells
189 (Figure 4F-I). Similarly, immunoblot analysis revealed low levels of PDC-E1α$^{Ser232/Ser293}$ in
190 XEN cells (Figure 4J), indicating that the PDC is active and would suggest higher
191 OXPHOS activity. However, expression analysis of the mitochondrial pyruvate carriers

192 *Mpc1* (Figure 4K), but not *Mpc2* (Figure 4L), showed significantly reduced expression in
193 XEN cells ($P < 0.0001$). Thus, despite having an active PDC, pyruvate in XEN cells fails
194 to enter the mitochondria, and instead is preferentially converted to lactate by the
195 enhanced LDHA activity (Figure 4A, B). These results would suggest that lactate
196 participates in specifying ES cells towards a XEN lineage.

197 **Promoting intracellular lactate enhances XEN differentiation**

198 Given the previous data highlighting a potential role for lactate in XEN cells (Figure
199 1-4), we sought to directly assess whether modulating lactate metabolism had an effect
200 on XEN induction *in vitro* (Figure 5). We adopted a previously defined chemical cocktail
201 (Anderson et al., 2017) to induce naïve mouse ES cells towards the XEN lineage.
202 Exogenous supplementation of LIF, Activin A and CHIR99021 (inhibitor of glycogen
203 synthase kinase 3) in the absence of insulin (Figure S3A) promotes differentiation towards
204 the XEN lineage as evident by elevated *Gata6* and *Dab2* transcript and low levels of
205 *Nanog* and *Oct4* (Figure S3B-E). To test whether lactate metabolism plays a role in XEN
206 differentiation, we used two approaches. In the first, three inhibitors were selected, two of
207 which would promote intracellular lactate accumulation (UK5099 and AZD3965), while
208 the other would promote pyruvate uptake into the mitochondria (Dichloroacetate, DCA).
209 In the second approach, media was supplemented with exogenous L-lactate and cells
210 were assessed for markers of pluripotency and XEN differentiation. UK5099 is a potent
211 pan MPC inhibitor that prevents pyruvate uptake into the mitochondria (Halestrap, 1975;
212 Vacanti et al., 2014), while AZD3965, a highly-specific MCT1 inhibitor, reduces lactate
213 secretion in human stem cells (Gu et al., 2016) and cancer cells (Polanski et al., 2014).
214 The latter was used since MCT1 is the predominant transporter responsible for exporting

215 lactate extracellularly in XEN cells (Figure 4D). Generally, neither UK5099, AZD3965 or
216 L-lactate affected *Oct* or *Nanog* expression (Figure 5C, F, G, J, K); however, *Oct4*
217 expression was slightly but significantly downregulated ($P < 0.05$) in ES cells cultured
218 under 2i-LIF and UK5099 conditions (Figure 5B). In contrast, DCA-treated ES cells
219 cultured with 2i-LIF had slightly elevated *Oct4* and *Nanog* expression when compared to
220 controls (Figure 5N, O).

221 Next, ES cells were induced towards the XEN lineage under control conditions or
222 treated with inhibitors or supplemented with L-lactate. ES cells treated with UK5099 in
223 XEN induction media were not viable after 48h post treatment (Figure 5D, E), while
224 surprisingly those cultured with either AZD3965 (Figure 5H, I) or supplemented with L-
225 lactate (Figure 5L, M) for 96h showed enhanced *Gata6* and *Dab2* expression when
226 compared to controls. Prolonged L-lactate supplementation induced cell death at 10 days
227 post treatment in cells differentiated towards the XEN lineage (data not shown).
228 Conversely, when ES cells were treated with DCA in XEN induction media, thereby
229 promoting pyruvate uptake into the mitochondria and reducing intracellular lactate, *Gata6*
230 and *Dab2* expression were significantly downregulated when compared to controls ($P <$
231 0.05, Figure 5P, Q). Therefore, promoting intracellular lactate accumulation enhanced
232 XEN induction *in vitro*, highlighting a novel role for lactate as a signaling molecule involved
233 in the differentiation of XEN cells.

234 # Discussion

235 We have shown previously that F9 embryonal carcinoma cells mimic the transition
236 to a XEN-like lineage when co-treated with retinoic acid and a cAMP analog, and more
237 importantly, these cells exhibited a metabolic phenotype reliant exclusively on glycolysis
238 (Gatie and Kelly, 2018). While recent reports have expanded on the metabolic profiles
239 observed in the early embryonic lineages (Choi et al., 2020; Zhou et al., 2012), a
240 comprehensive analysis of the metabolites and their roles during development remains
241 lacking. Our data indicates that feeder-free XEN cells are sensitive to glycolytic inhibition
242 when compared with OXPHOS inhibition (Figure 1A, B). This phenomenon is also
243 observed in mouse primed stem cells, human stem cells (Zhou et al., 2012) and canine
244 epiblast stem cells (Tobias et al., 2018), suggesting that these characteristics are
245 adaptive mechanisms linked to a developmental stage. Furthermore, XEN cells possess
246 altered glycolytic enzyme levels involved in pyruvate and lactate homeostasis (Figure 4).
247 Recent reports suggested that XEN cells rely on OXPHOS metabolism for energetic
248 needs (Choi et al., 2020); however, the developmental stage and culture condition of XEN
249 cells may influence their metabolic profile. For instance, primitive endoderm cells are
250 present within the ICM at 3.5 days post fertilization and they further commit into parietal
251 and visceral endoderm cells shortly after implantation. A similar phenomenon is observed
252 between preimplantation naïve *versus* post-implantation primed ES cells, which display
253 distinct metabolic profiles (Zhou et al., 2012), suggesting that XEN cells may exhibit a
254 unique metabolic signature depending on their developmental stage. In addition, the
255 localization of XEN cells varies depending on the stage of development, where primitive
256 endoderm cells reside within the ICM, visceral endoderm cells surround the epiblast while

257 parietal endoderm cells interact with trophoblast stem cells and undergo an epithelial-to-
258 mesenchymal transition and migrate along the inner surface of the trophectoderm (Hogan
259 et al., 1980). Therefore, the precise identity of these XEN cells and their interaction with
260 the microenvironment may influence their metabolic needs. Lastly, culture conditions vary
261 between trophoblast, ES and XEN cells, and its known that the latter can be derived using
262 various culture conditions and supplements (Anderson et al., 2017; Cho et al., 2012;
263 Fujikura et al., 2002; He et al., 2020; Kunath et al., 2005; McDonald et al., 2014; Niakan
264 et al., 2013; Paca et al., 2012; Shimosato et al., 2007; Soprano et al., 2007; Wamaitha et
265 al., 2015). Together, the ability to derive XEN cells by various means would contribute to
266 their heterogeneity (Kunath et al., 2005; Paca et al., 2012) and potentially affect the
267 metabolic profile of these cells. For example, XEN cells can be generated by the
268 overexpression of *Gata4* in ES cells (Fujikura et al., 2002; Wamaitha et al., 2015) or
269 reprogramming fibroblasts using a chemical cocktail (He et al., 2020). While both methods
270 result in the establishment of XEN cells, *Gata4*-induced ES cells display gradual reduction
271 in hexokinase 2 (HK2) and glucose transporter 1 (GLUT1) levels (Mulvey et al., 2015),
272 while XEN cells reprogrammed from fibroblasts display elevated *Hk2* and *Glut1* levels
273 (He et al., 2020). Together, these differences highlight the metabolic complexity and
274 plasticity of all cells in the developing embryo, and in XEN cells specifically.

275 As the embryo develops its metabolic needs shift to meet energetic demands for
276 growth and development and this metabolic rewiring is dependent on extrinsic and
277 intrinsic cues. The blastocyst resides in a hypoxic environment, with oxygen tension
278 dropping significantly during implantation (Fischer and Bavister, 1993). This hypoxic
279 environment results in the stabilization of hypoxia-inducible factor one alpha (HIF1α),

280 resulting in the increase in enzymes shifting the metabolic profile towards glycolysis.
281 During implantation, however, angiogenesis promotes reoxygenation of the embryo
282 triggering a switch to OXPHOS. Despite residing in a similar environment, trophoblast
283 stem cells rely on OXPHOS metabolism, largely to fuel the sodium/potassium ion pumps
284 required for blastocoel expansion (Houghton et al., 2003). While extrinsic factors such as
285 the microenvironment are important, intrinsic factors play a key role in remodeling
286 metabolic needs to meet developmental programs. For example, naïve ES cells are
287 metabolically flexible and utilize both glycolysis and OXPHOS metabolism. However, the
288 transition to a primed state is marked by a switch to glycolytic metabolism, which is largely
289 due to HIF1α stabilization within the cell (Zhou et al., 2012). While changes in the levels
290 of metabolic enzymes play a role in remodelling cellular metabolism, the metabolites
291 resulting from the activity of these enzymes are instrumental in regulating pluripotency
292 and/or differentiation. Our study is the first to provide a comprehensive snapshot of the
293 intracellular metabolite profile of feeder-free XEN cells and reveals how elevated levels
294 of key metabolites, mainly lactate, influence differentiation.

295 Lactate, the primary source of carbon for the TCA cycle in both normal and cancer
296 tissues (Hui et al., 2017), is generated by the activity of LDHA, reportedly enriched in XEN
297 cells (Figure 4A, B). Since lactate can be converted to pyruvate by LDHB, the
298 stoichiometric ratio between the two isoforms dictates the fate of pyruvate and lactate. In
299 addition, the oxidation of pyruvate by the PDC is required for its conversion to acetyl CoA,
300 and the activity of the complex is regulated by the PDK family. Despite detecting elevated
301 intracellular (Figure 2C) and extracellular (Figure 4C) lactate levels in XEN cells, the PDC
302 was not phosphorylated and is therefore active in XEN cells (Figure 4J). While reduced

303 expression of *Mpc1* was found in XEN cells (Figure 4K), which may explain the rerouting
304 of pyruvate to lactate, PDC is known to have moonlighting abilities and can translocate to
305 the nucleus where it generates acetyl CoA for acetylation of H3K9 and H3K18 (Sutendra
306 et al., 2014). Thus, since total lysates were used to analyze the phosphorylation status of
307 the PDC in ES and XEN cells, it is possible that a higher proportion of the active complex
308 is nuclear and not mitochondrial. Nevertheless, since elevated intracellular lactate levels
309 were found in XEN cells (Figure 2C), it was hypothesized that lactate plays a crucial role
310 during XEN differentiation. Chemical inhibition to promote intracellular lactate
311 accumulation (Figure 5H, I) or supplementation of XEN induction media with L-lactate
312 (Figure 5L, M) showed enhanced XEN differentiation. Surprisingly, blocking pyruvate
313 uptake into the mitochondria using UK5099 led to cell mortality (Figure 5D, E).
314 Alternatively, promoting pyruvate uptake into the mitochondria by inhibiting PDKs resulted
315 in significant reduction in XEN differentiation (Figure 5P, Q). Therefore, our results
316 support the notion that maintaining intracellular lactate levels potentiates ES cells towards
317 a XEN lineage. Since lactate can stabilize HIF1α and promote a glycolytic phenotype (De
318 Saedeleer et al., 2012), the lactate-HIF1α axis may provide a mechanism for XEN
319 differentiation. In addition, lactate can also inhibit histone deacetylases (Latham et al.,
320 2012), and in conjunction with active PDC (Figure 4J), promote hyperacetylation, which
321 we observed in XEN cells (data not shown). Thus, it appears lactate is a key player linking
322 metabolism with epigenetic factors and transcription. These links provide insight into the
323 role lactate plays in directing the differentiation of XEN cells, and together they
324 underscore the importance of how the metabolic profile directs lineage commitment within
325 the mouse early embryo.

326 # Experimental Procedures

327 **ES, XEN and cXEN Cell Culture**

328 The ES-E14TG2a embryonic stem (ES) cells were obtained from the University of
329 California, Davis. ES cells were cultured feeder-free on 0.1% gelatin-coated tissue culture
330 plates in ES media: 50/50 neurobasal/DMEM-F12 media (Thermo Fisher), 1X N2
331 supplement (Thermo Fisher), 0.5X B27 (without retinoic acid; Thermo Fisher), 2mM
332 GlutaMAX™ (Thermo Fisher), 0.1mM β-mercaptoethanol (Thermo Fisher), 100U/ml units
333 of LIF (Millipore-Sigma), 3μM CHIR99021 (ApexBio) and 1μM PD 0325901 (ApexBio).
334 ES cells were passaged every 3–4 days using Accutase (Thermo Fisher) and used to
335 passage 30. ES media was changed daily to maintain optimal growth and reduce
336 spontaneous differentiation. E4 extraembryonic endoderm (XEN) cells, generously
337 donated from Dr. Janet Rossant, University of Toronto (Kunath et al., 2005), were cultured
338 in RPMI1640 media (Thermo Fisher) supplemented with 15% fetal bovine serum (Thermo
339 Fisher), 2mM GlutaMAX™ and 0.1mM β-mercaptoethanol. XEN cells were passaged
340 every 2–4 days using TrypLE Express (Thermo Fisher) up to passage 20.

341 Chemically induced XEN (cXEN) differentiation was performed following a previously
342 established protocol (Anderson et al., 2017). Briefly, ES cells were seeded onto 0.1%
343 gelatin-coated tissue culture plates in base XEN media (RPMI1640 media, 0.5X B27
344 without insulin, 2mM GlutaMAX™ and 0.1mM β-mercaptoethanol) for 2 days. To induce
345 XEN differentiation, base XEN media was supplemented with 100U/ml units of LIF, 3μM
346 CHIR99021 and 20ng/ml Activin A (R&D Systems), which was changed every 2 days. All
347 lines were grown at 37°C and 5% CO_2 and checked for chromosomal abnormalities and
348 mycoplasma (Dobrovolny and Bess, 2011) at the beginning of the project.

349 **RNA Isolation, cDNA synthesis and qRT-PCR analysis**

350 RNA was extracted from cells using QIAshredder/RNAeasy Mini kit (Qiagen) and reverse
351 transcribed into cDNA using the High-Capacity cDNA Reverse Transcription kit (Thermo
352 Fisher). For quantitative RT-PCR, reactions contained 500nM of forward and reverse
353 primers (Gatie and Kelly, 2018), SensiFAST SYBR Mix (FroggaBio), and cDNA.
354 Reactions were run on a CFX Connect Real-Time PCR detection system (Bio-Rad), and
355 results presented using the comparative cycle threshold ($2^{-\Delta\Delta Ct}$) method with *Rpl14*
356 serving as the internal control.

357 **RNA Sequencing Analysis**

358 Total RNA was extracted as described previously and quantified using a NanoDrop 2000
359 spectrophotometer (Thermo Fisher) and Agilent 2100 bioanalyzer (Agilent Technologies).
360 Library construction and sequencing were performed using the BGISEQ-500 platform
361 (Beijing Genome Institute). Clean reads were mapped to a reference genome using
362 Bowtie2 (Langmead and Salzberg, 2012) and gene expression levels were calculated
363 with RSEM (Li and Dewey, 2011). Differentially expressed genes were detected with
364 DEseq2 (Love et al., 2014) with fold change ≥ 2.0 and $P \leq 0.0001$, and GO-term
365 enrichment and KEGG analyses were conducted using David v6.8 (Huang da et al.,
366 2009a, b).

367 **Protein extraction, quantification and immunoblot analysis**

368 Total cell lysates were harvested using RIPA buffer supplemented with protease and
369 phosphatase inhibitors (Thermo Fisher). Protein concentrations were quantified using a
370 DC™ protein assay (Bio-Rad). Approximately 5–20μg of protein was separated on 5–15%
371 polyacrylamide gels at 100V, then transferred onto PVDF membranes (Bio-Rad)

372 overnight at 4°C at 20V. Membranes were washed in TBS-T with 0.1% Tween-20 and
373 blocked with 5% skim milk powder for 30 minutes at room temperature with gentle shaking.
374 Membranes were probed with primary antibodies (Gatie and Kelly, 2018) overnight at 4°C
375 followed by washes with TBS-T and secondary antibody incubation for 2 hours at room
376 temperature. Images were captured using a ChemiDoc™ Touch Imaging System (Bio-
377 Rad).

378 **Proteomic Analysis**

379 Sample preparation, handling and quantification were performed according to (Cooper et
380 al., 2018). Briefly, cells were pelleted and 50µg of protein was quantified by ionic
381 detergent compatible Pierce 660nm Protein Assay Reagent (Thermo Fisher) in 8M Urea,
382 50mM ammonium bicarbonate, 10mM dithiothreitol, and 2% SDS lysis buffer. Lysates
383 were sonicated, reduced and alkylated followed by precipitation in chloroform/methanol
384 (Wessel and Flugge, 1984), and digested samples were resuspended in 0.1% formic acid
385 in preparation for LC-MS/MS. One microgram of tryptic peptides was injected into a
386 Waters nano-Acquity HPLC system (Waters, Milford, MA) coupled to an ESI Orbitrap
387 mass spectrometer (Orbitrap Elite or QExactive, ThermoFisher Scientific). MS raw files
388 were examined using MaxQuant (1.6.5.0) and the Human Uniprot database. Bioinformatic
389 analyses were performed in Perseus (1.5.8.5), and statistical analyses performed using
390 multiple sample t-test with a permutation FDR set at 0.05. GO-term enrichment and
391 KEGG analyses were conducted using David v6.8 (Huang da et al., 2009a, b).

392 **Detection of Total ATP levels**

393 Total ATP levels were measured using the CellTiter-Glo® Luminescent Cell Viability
394 Assay (Promega). Cells were detached and re-suspended in media and aliquoted into

395 96-well plate. Cells were lysed in CellTiter-Glo® reagent, incubated in the dark for 10
396 minutes, and luminance recorded using a Modulus™ II microplate multimode system
397 (Promega).

398 **Detection of Extracellular Lactate Levels**

399 Cells were cultured under normal conditions until reaching 70% confluency. Media from
400 each cell population was collected, centrifuge at 14000g at 4°C for 10 minutes and
401 analyzed using a BioProfile®400 Chemical Analyzer (Nova Biochemical), at the GCRC
402 Metabolomics Core Facility, McGill University. Values were normalized to protein
403 concentrations.

404 **Metabolomic Analysis**

405 Three million cells, cultured for 4 days under normal conditions, per sample were used
406 for extraction and analysis. Samples were analyzed for metabolites involved in glycolysis,
407 and TCA cycle, as well as amino acids, fatty acid and lipids. Sample preparation, handling
408 and quantification were carried out as in (Yuan et al., 2012) by The Analytical Facility for
409 Bioactive Molecules, The Hospital for Sick Children, Toronto, Canada. Briefly, cells were
410 harvested in 80% methanol (vol/vol) solution, centrifuged at 14,000g for 5 minutes at 4°C.
411 Samples were aliquoted and lyophilized prior to injection. Approximately 20µl of LC/MS
412 grade water was used to resuspend samples and 5–10µl was injected into a LC-MS/MS
413 system which was a SCIEX 5500 QTRAP mass spectrometer (SCIEX) coupled with an
414 Agilent 1290 HPLC stack (Agilent Technologies). MultiQuant (v3.0; SCIEX) was used for
415 analysis,

416 **Data and Code Availability**

417 Data files can be obtained from accession number GEO: GSE159855.

418 **Statistical Analysis**

419 All values are presented as mean ± SEM from at least three biological experiments. In
420 some instances (TEM experiments), three technical replicates were also included.
421 Comparisons between two groups were performed using Student's t-test, while
422 comparisons between three or more groups were done using an ANOVA test followed by
423 Tukey's honest significant difference test. All graphs and statistics were generated using
424 Prism (v8.4.3). *P*-values were considered significant at $^{*}P<0.05$, $^{**}P<0.01$, $^{***}P<0.001$,
425 $^{****}P<0.0001$.

Acknowledgments:

This work was supported by discovery grant from the Natural Sciences and Engineering Research Council (NSERC R2615A02) to G.M.K. G.A.L. was supported by NSERC and Canadian Foundation for Innovation (CFI). M.I.G was supported by NSERC CGS-D scholarship and the Child Health Research Institute. The authors acknowledge the assistance from the GCRC Metabolomics core facilities, which is supported by grants from CFI, Canadian Institutes of Health Research, and Terry Fox Research Institute. The authors wish to thank Ashley St. Pierre of The Analytical Facility for Bioactive Molecules, The Hospital for Sick Children, Toronto, Canada for assistance with metabolite identification and analysis. The authors would like to thank Rached Alkallas (McGill) for assistance with RNA sequencing and data visualization.

Author Contributions:

MIG conceptualized, designed, performed the experiments and wrote the manuscript. TTC performed and analyzed proteomics experiment.

GAL managed the proteomic component of the project.

GMK was involved with MIG and the experimental design and supervised the research.

Declaration of Interests:

The authors declare no interest.

444 **References:**

445 Anderson, K.G.V., Hamilton, W.B., Roske, F.V., Azad, A., Knudsen, T.E., Canham,
446 M.A., Forrester, L.M., and Brickman, J.M. (2017). Insulin fine-tunes self-renewal
447 pathways governing naive pluripotency and extra-embryonic endoderm. Nat Cell Biol
448 *19*, 1164-1177.
449 Baksh, S.C., Todorova, P.K., Gur-Cohen, S., Hurwitz, B., Ge, Y., Novak, J.S.S.,
450 Tierney, M.T., Dela Cruz-Racelis, J., Fuchs, E., and Finley, L.W.S. (2020). Extracellular
451 serine controls epidermal stem cell fate and tumour initiation. Nat Cell Biol *22*, 779-790.
452 Brons, I.G., Smithers, L.E., Trotter, M.W., Rugg-Gunn, P., Sun, B., Chuva de Sousa
453 Lopes, S.M., Howlett, S.K., Clarkson, A., Ahrlund-Richter, L., Pedersen, R.A.*, et al.*
454 (2007). Derivation of pluripotent epiblast stem cells from mammalian embryos. Nature
455 *448*, 191-195.
456 Cho, L.T., Wamaitha, S.E., Tsai, I.J., Artus, J., Sherwood, R.I., Pedersen, R.A.,
457 Hadjantonakis, A.K., and Niakan, K.K. (2012). Conversion from mouse embryonic to
458 extra-embryonic endoderm stem cells reveals distinct differentiation capacities of
459 pluripotent stem cell states. Development *139*, 2866-2877.
460 Choi, J., Seo, B.J., La, H., Yoon, S.H., Hong, Y.J., Lee, J.H., Chung, H.M., Hong, K.,
461 and Do, J.T. (2020). Comparative analysis of the mitochondrial morphology, energy
462 metabolism, and gene expression signatures in three types of blastocyst-derived stem
463 cells. Redox Biol *30*, 101437.
464 Comes, S., Gagliardi, M., Laprano, N., Fico, A., Cimmino, A., Palamidessi, A., De
465 Cesare, D., De Falco, S., Angelini, C., Scita, G.*, et al.* (2013). L-Proline induces a

466 mesenchymal-like invasive program in embryonic stem cells by remodeling H3K9 and
467 H3K36 methylation. Stem Cell Reports *1*, 307-321.
468 Cooper, T.T., Sherman, S.E., Kuljanin, M., Bell, G.I., Lajoie, G.A., and Hess, D.A.
469 (2018). Inhibition of Aldehyde Dehydrogenase-Activity Expands Multipotent Myeloid
470 Progenitor Cells with Vascular Regenerative Function. Stem Cells *36*, 723-736.
471 Davidson, K.C., Mason, E.A., and Pera, M.F. (2015). The pluripotent state in mouse and
472 human. Development *142*, 3090-3099.
473 De Saedeleer, C.J., Copetti, T., Porporato, P.E., Verrax, J., Feron, O., and Sonveaux,
474 P. (2012). Lactate activates HIF-1 in oxidative but not in Warburg-phenotype human
475 tumor cells. PLoS One *7*, e46571.
476 Dobrovolny, P.L., and Bess, D. (2011). Optimized PCR-based detection of mycoplasma.
477 J Vis Exp.
478 Evans, M.J., and Kaufman, M.H. (1981). Establishment in culture of pluripotential cells
479 from mouse embryos. Nature *292*, 154-156.
480 Fischer, B., and Bavister, B.D. (1993). Oxygen tension in the oviduct and uterus of
481 rhesus monkeys, hamsters and rabbits. J Reprod Fertil *99*, 673-679.
482 Folmes, C.D., Nelson, T.J., Martinez-Fernandez, A., Arrell, D.K., Lindor, J.Z., Dzeja,
483 P.P., Ikeda, Y., Perez-Terzic, C., and Terzic, A. (2011). Somatic oxidative bioenergetics
484 transitions into pluripotency-dependent glycolysis to facilitate nuclear reprogramming.
485 Cell Metab *14*, 264-271.
486 Fujikura, J., Yamato, E., Yonemura, S., Hosoda, K., Masui, S., Nakao, K., Miyazaki Ji,
487 J., and Niwa, H. (2002). Differentiation of embryonic stem cells is induced by GATA
488 factors. Genes Dev *16*, 784-789.

489 Gatie, M.I., and Kelly, G.M. (2018). Metabolic profile and differentiation potential of
490 extraembryonic endoderm-like cells. Cell Death Discov *4*, 42.
491 Gu, W., Gaeta, X., Sahakyan, A., Chan, A.B., Hong, C.S., Kim, R., Braas, D., Plath, K.,
492 Lowry, W.E., and Christofk, H.R. (2016). Glycolytic Metabolism Plays a Functional Role
493 in Regulating Human Pluripotent Stem Cell State. Cell Stem Cell *19*, 476-490.
494 Halestrap, A.P. (1975). The mitochondrial pyruvate carrier. Kinetics and specificity for
495 substrates and inhibitors. Biochem J *148*, 85-96.
496 He, X., Chi, G., Li, M., Xu, J., Zhang, L., Song, Y., Wang, L., and Li, Y. (2020).
497 Characterisation of extraembryonic endoderm-like cells from mouse embryonic
498 fibroblasts induced using chemicals alone. Stem Cell Res Ther *11*, 157.
499 Hogan, B.L., Cooper, A.R., and Kurkinen, M. (1980). Incorporation into Reichert's
500 membrane of laminin-like extracellular proteins synthesized by parietal endoderm cells
501 of the mouse embryo. Dev Biol *80*, 289-300.
502 Houghton, F.D., Humpherson, P.G., Hawkhead, J.A., Hall, C.J., and Leese, H.J. (2003).
503 Na+, K+, ATPase activity in the human and bovine preimplantation embryo. Dev Biol
504 *263*, 360-366.
505 Huang da, W., Sherman, B.T., and Lempicki, R.A. (2009a). Bioinformatics enrichment
506 tools: paths toward the comprehensive functional analysis of large gene lists. Nucleic
507 Acids Res *37*, 1-13.
508 Huang da, W., Sherman, B.T., and Lempicki, R.A. (2009b). Systematic and integrative
509 analysis of large gene lists using DAVID bioinformatics resources. Nat Protoc *4*, 44-57.

510 Hui, S., Ghergurovich, J.M., Morscher, R.J., Jang, C., Teng, X., Lu, W., Esparza, L.A.,
511 Reya, T., Le, Z., Yanxiang Guo, J.*, et al.* (2017). Glucose feeds the TCA cycle via
512 circulating lactate. Nature *551*, 115-118.
513 Kunath, T., Arnaud, D., Uy, G.D., Okamoto, I., Chureau, C., Yamanaka, Y., Heard, E.,
514 Gardner, R.L., Avner, P., and Rossant, J. (2005). Imprinted X-inactivation in extra-
515 embryonic endoderm cell lines from mouse blastocysts. Development *132*, 1649-1661.
516 Langmead, B., and Salzberg, S.L. (2012). Fast gapped-read alignment with Bowtie 2.
517 Nat Methods *9*, 357-359.
518 Latham, T., Mackay, L., Sproul, D., Karim, M., Culley, J., Harrison, D.J., Hayward, L.,
519 Langridge-Smith, P., Gilbert, N., and Ramsahoye, B.H. (2012). Lactate, a product of
520 glycolytic metabolism, inhibits histone deacetylase activity and promotes changes in
521 gene expression. Nucleic Acids Res *40*, 4794-4803.
522 Li, B., and Dewey, C.N. (2011). RSEM: accurate transcript quantification from RNA-Seq
523 data with or without a reference genome. BMC Bioinformatics *12*, 323.
524 Love, M.I., Huber, W., and Anders, S. (2014). Moderated estimation of fold change and
525 dispersion for RNA-seq data with DESeq2. Genome Biol *15*, 550.
526 Mali, P., Chou, B.K., Yen, J., Ye, Z., Zou, J., Dowey, S., Brodsky, R.A., Ohm, J.E., Yu,
527 W., Baylin, S.B.*, et al.* (2010). Butyrate greatly enhances derivation of human induced
528 pluripotent stem cells by promoting epigenetic remodeling and the expression of
529 pluripotency-associated genes. Stem Cells *28*, 713-720.
530 Mathieu, J., and Ruohola-Baker, H. (2017). Metabolic remodeling during the loss and
531 acquisition of pluripotency. Development *144*, 541-551.

532 McDonald, A.C., Biechele, S., Rossant, J., and Stanford, W.L. (2014). Sox17-mediated
533 XEN cell conversion identifies dynamic networks controlling cell-fate decisions in
534 embryo-derived stem cells. Cell Rep *9*, 780-793.
535 Mulvey, C.M., Schroter, C., Gatto, L., Dikicioglu, D., Fidaner, I.B., Christoforou, A.,
536 Deery, M.J., Cho, L.T., Niakan, K.K., Martinez-Arias, A.*, et al.* (2015). Dynamic
537 Proteomic Profiling of Extra-Embryonic Endoderm Differentiation in Mouse Embryonic
538 Stem Cells. Stem Cells *33*, 2712-2725.
539 Niakan, K.K., Schrode, N., Cho, L.T., and Hadjantonakis, A.K. (2013). Derivation of
540 extraembryonic endoderm stem (XEN) cells from mouse embryos and embryonic stem
541 cells. Nat Protoc *8*, 1028-1041.
542 Nichols, J., Evans, E.P., and Smith, A.G. (1990). Establishment of germ-line-competent
543 embryonic stem (ES) cells using differentiation inhibiting activity. Development *110*,
544 1341-1348.
545 Nowotschin, S., Hadjantonakis, A.K., and Campbell, K. (2019). The endoderm: a
546 divergent cell lineage with many commonalities. Development *146*.
547 Paca, A., Seguin, C.A., Clements, M., Ryczko, M., Rossant, J., Rodriguez, T.A., and
548 Kunath, T. (2012). BMP signaling induces visceral endoderm differentiation of XEN cells
549 and parietal endoderm. Dev Biol *361*, 90-102.
550 Parenti, A., Halbisen, M.A., Wang, K., Latham, K., and Ralston, A. (2016). OSKM
551 Induce Extraembryonic Endoderm Stem Cells in Parallel to Induced Pluripotent Stem
552 Cells. Stem Cell Reports *6*, 447-455.

553 Polanski, R., Hodgkinson, C.L., Fusi, A., Nonaka, D., Priest, L., Kelly, P., Trapani, F.,
554 Bishop, P.W., White, A., Critchlow, S.E.*, et al.* (2014). Activity of the monocarboxylate
555 transporter 1 inhibitor AZD3965 in small cell lung cancer. Clin Cancer Res *20*, 926-937.
556 Ryu, J.M., and Han, H.J. (2011). L-threonine regulates G1/S phase transition of mouse
557 embryonic stem cells via PI3K/Akt, MAPKs, and mTORC pathways. J Biol Chem *286*,
558 23667-23678.
559 Seo, B.J., Choi, J., La, H., Habib, O., Choi, Y., Hong, K., and Do, J.T. (2020). Role of
560 mitochondrial fission-related genes in mitochondrial morphology and energy metabolism
561 in mouse embryonic stem cells. Redox Biol *36*, 101599.
562 Shimosato, D., Shiki, M., and Niwa, H. (2007). Extra-embryonic endoderm cells derived
563 from ES cells induced by GATA factors acquire the character of XEN cells. BMC Dev
564 Biol *7*, 80.
565 Soprano, D.R., Teets, B.W., and Soprano, K.J. (2007). Role of retinoic acid in the
566 differentiation of embryonal carcinoma and embryonic stem cells. Vitam Horm *75*, 69-
567 95.
568 Sutendra, G., Kinnaird, A., Dromparis, P., Paulin, R., Stenson, T.H., Haromy, A.,
569 Hashimoto, K., Zhang, N., Flaim, E., and Michelakis, E.D. (2014). A nuclear pyruvate
570 dehydrogenase complex is important for the generation of acetyl-CoA and histone
571 acetylation. Cell *158*, 84-97.
572 Tobias, I.C., Isaac, R.R., Dierolf, J.G., Khazaee, R., Cumming, R.C., and Betts, D.H.
573 (2018). Metabolic plasticity during transition to naive-like pluripotency in canine embryo-
574 derived stem cells. Stem Cell Res *30*, 22-33.

575 Tsogtbaatar, E., Landin, C., Minter-Dykhouse, K., and Folmes, C.D.L. (2020). Energy
576 Metabolism Regulates Stem Cell Pluripotency. Front Cell Dev Biol *8*, 87.
577 Vacanti, N.M., Divakaruni, A.S., Green, C.R., Parker, S.J., Henry, R.R., Ciaraldi, T.P.,
578 Murphy, A.N., and Metallo, C.M. (2014). Regulation of substrate utilization by the
579 mitochondrial pyruvate carrier. Mol Cell *56*, 425-435.
580 Wamaitha, S.E., del Valle, I., Cho, L.T., Wei, Y., Fogarty, N.M., Blakeley, P., Sherwood,
581 R.I., Ji, H., and Niakan, K.K. (2015). Gata6 potently initiates reprograming of pluripotent
582 and differentiated cells to extraembryonic endoderm stem cells. Genes Dev *29*, 1239-
583 1255.
584 Wang, J., Alexander, P., Wu, L., Hammer, R., Cleaver, O., and McKnight, S.L. (2009).
585 Dependence of mouse embryonic stem cells on threonine catabolism. Science *325*,
586 435-439.
587 Wessel, D., and Flugge, U.I. (1984). A method for the quantitative recovery of protein in
588 dilute solution in the presence of detergents and lipids. Anal Biochem *138*, 141-143.
589 Yanes, O., Clark, J., Wong, D.M., Patti, G.J., Sanchez-Ruiz, A., Benton, H.P., Trauger,
590 S.A., Desponts, C., Ding, S., and Siuzdak, G. (2010). Metabolic oxidation regulates
591 embryonic stem cell differentiation. Nat Chem Biol *6*, 411-417.
592 Ying, Q.L., Wray, J., Nichols, J., Batlle-Morera, L., Doble, B., Woodgett, J., Cohen, P.,
593 and Smith, A. (2008). The ground state of embryonic stem cell self-renewal. Nature *453*,
594 519-523.
595 Yuan, M., Breitkopf, S.B., Yang, X., and Asara, J.M. (2012). A positive/negative ion-
596 switching, targeted mass spectrometry-based metabolomics platform for bodily fluids,
597 cells, and fresh and fixed tissue. Nat Protoc *7*, 872-881.

598 Zhang, J., Nuebel, E., Daley, G.Q., Koehler, C.M., and Teitell, M.A. (2012). Metabolic
599 regulation in pluripotent stem cells during reprogramming and self-renewal. Cell Stem
600 Cell *11*, 589-595.
601 Zhou, W., Choi, M., Margineantu, D., Margaretha, L., Hesson, J., Cavanaugh, C., Blau,
602 C.A., Horwitz, M.S., Hockenbery, D., Ware, C.*, et al.* (2012). HIF1alpha induced switch
603 from bivalent to exclusively glycolytic metabolism during ESC-to-EpiSC/hESC transition.
604 EMBO J *31*, 2103-2116.
605

606 # Figure Legends:

607 **Figure 1. XEN cells are more sensitive to glycolytic inhibition.**

608 (A) Representative phase contrast images of ES and XEN cells cultured under control,
609 50mM 2-DG, and 2.5μM oligomycin. Solid arrows are indicative of round XEN morphology.
610 Dashed arrows are indicative of stellate XEN morphology. Scale bars = 100μm.

611 (B) Relative cell viability of ES and XEN cells under control, 50mM 2-DG and 2.5μM
612 oligomycin conditions.

613 (C) Total ATP levels in ES and XEN cells under control, 50mM 2-DG and 2.5μM
614 oligomycin conditions. (n = three biological replicates, ns = not significant, $^{**}P < 0.01$, $^{***}P$
615 <0.001).

616 **Figure 2. Intracellular metabolomic analysis of ES and XEN cells.**

617 (A) Volcano plots of differentially expressed metabolites from untargeted LC/GC-MS/MS
618 metabolomics of ES and XEN cells cultured under normal conditions. (fold change > 1
619 and $P < 0.05$). Metabolites enriched in ES cells are highlighted in purple (38 metabolites)
620 and metabolites enriched in XEN cells are highlighted in orange (105 metabolites).

621 (B, C) Levels of key intracellular metabolites generated by glycolysis, TCA cycle, and
622 amino acid detected by targeted LC/GC-MS/MS analysis of ES and XEN cells cultured
623 under normal conditions. Metabolites are expressed in ng and were normalized to cell
624 number. (n = three biological replicates, ns = not significant, $^{*}P < 0.05$, $^{**}P < 0.01$).

625 **Figure 3. Bulk transcriptomic and proteomic analysis of ES and XEN cells.**

626 (A) Volcano plots of differentially expressed genes from bulk RNA sequencing of ES and
627 XEN cells cultured under normal conditions. (fold change > 2 and adjusted $P < 0.01$).

628 Genes enriched in ES cells are highlighted in purple (2742 genes) and genes enriched in
629 XEN cells are highlighted in orange (1716 genes).
630 (B) Volcano plots of differentially expressed proteins from bulk proteomics of ES and XEN
631 cells cultured under normal conditions. (fold change > 2 and adjusted $P < 0.01$). Proteins
632 abundant in ES cells are highlighted in purple (165 proteins) and proteins abundant in
633 XEN cells are highlighted in orange (298 proteins).
634 (C) Dot plot representing enriched KEGG pathways in ES cells from transcriptomic
635 dataset.
636 (D) Dot plot representing enriched KEGG pathways in ES cells from proteomic dataset.
637 (E) Venn diagram of common targets from both transcriptomic and proteomic datasets
638 for specific KEGG pathways.
639 (F) Dot plot representing enriched KEGG pathways in XEN cells from transcriptomic
640 dataset.
641 (G) Dot plot representing enriched KEGG pathways in XEN cells from proteomic dataset.
642 **Figure 4. Levels of enzymes involved in pyruvate metabolism in ES and XEN cells.**
643 (A) Bar graph of qRT-PCR analysis of *Ldha/Ldhb* ratio in ES and XEN cells. *Rpl14* was
644 used a constitutive gene for qRT-PCR. (n = three biological replicates, $^{**}P < 0.01$).
645 (B) Representative immunoblot analysis showing levels of LDHA and LDHB in ES and
646 XEN cells. β-ACTIN served as a loading control. (n = three biological replicates).
647 (C) Bar graph of extracellular quantification of lactate levels in ES and XEN cells by
648 BioProfile®400 Chemical Analyzer. (n = three biological replicates, $^{*}P < 0.05$).
649 (D-E) Bar graph of expression level of *Mct1* and *Mct4* in ES and XEN cells. FPKM was
650 used for RNAseq data. (n = three biological replicates, $^{****}P < 0.0001$).

651 (F-I) Bar graph of FPKM of *Pdk1-4* in ES and XEN cells. (n = three biological replicates,
652 ns = not significant, $^{**}P$ <0.01, $^{****}P$ <0.0001).
653 (J) Representative immunoblot analysis showing levels of PDK1, PDK4, PDC-E1α^{pSer232},
654 PDC-E1α^{pSer293}, and PDC-E1α in ES and XEN cells. (n = three biological replicates).
655 (K-L) Bar graph of expression level of *Mpc1* and *Mpc2* in ES and XEN cells. FPKM was
656 used for RNAseq data. (n = three biological replicates, $^{***}P$ <0.001).
657 **Figure 5. Intracellular lactate enhances XEN differentiation *in vitro*.**
658 (A) Schematic diagram of glucose metabolism and the metabolic enzymes involved.
659 Green is indicative of treatments that increase intracellular lactate and red is indicative of
660 treatment that decrease intracellular lactate.
661 (B-C) Bar graph of expression level of *Oct4* and *Nanog* in ES cells in 2i-LIF with or without
662 50μM UK5099 for 48h. *Rpl14* was used a constitutive gene for qRT-PCR. (n = three
663 biological replicates, $^{*}P$ <0.05).
664 (D-E) Bar graph of expression level of *Gata6* and *Dab2* in ES cells induced towards a
665 XEN lineage with or without 50μM UK5099 for 96h. *Rpl14* was used a constitutive gene
666 for qRT-PCR. (n = three biological replicates, $^{*}P$ <0.05).
667 (F-G) Bar graph of expression level of *Oct4* and *Nanog* in ES cells in 2i-LIF with or without
668 250nM AZD3965 for 48h. *Rpl14* was used a constitutive gene for qRT-PCR. (n = three
669 biological replicates).
670 (H-I) Bar graph of expression level of *Gata6* and *Dab2* in ES cells induced towards a XEN
671 lineage with or without 250nM AZD3965 for 96h. *Rpl14* was used a constitutive gene for
672 qRT-PCR. (n = three biological replicates, $^{*}P$ <0.05).

673 (J-K) Bar graph of expression level of *Oct4* and *Nanog* in ES cells in 2i-LIF with or without
674 5mM L-lactate for 48h. *Rpl14* was used a constitutive gene for qRT-PCR. (n = three
675 biological replicates).
676 (L-M) Bar graph of expression level of *Gata6* and *Dab2* in ES cells induced towards a
677 XEN lineage with or without 5mM L-lactate for 96h. *Rpl14* was used a constitutive gene
678 for qRT-PCR. (n = three biological replicates, $^{*}P$ <0.05).
679 (N-O) Bar graph of expression level of *Oct4* and *Nanog* in ES cells in 2i-LIF with or without
680 5mM DCA for 48h. *Rpl14* was used a constitutive gene for qRT-PCR. (n = three biological
681 replicates, $^{*}P$ <0.05, $^{**}P$ <0.01).
682 (P-Q) Bar graph of expression level of *Gata6* and *Dab2* in ES cells induced towards a
683 XEN lineage with or without 5mM DCA for 96h. *Rpl14* was used a constitutive gene for
684 qRT-PCR. (n = three biological replicates, $^{*}P$ <0.05).
685 **Figure S1. Morphological and molecular analysis of ES and XEN cells *in vitro*.**
686 (A) A representative phase contrast micrograph of ES and XEN cells cultured under
687 maintenance conditions under free-feeder conditions.
688 (B) Immunoblot analysis of OCT4 (pluripotency marker) and DAB2, GATA6, and
689 KERATIN-8 (extraembryonic endoderm markers). β-ACTIN served as a loading control.
690 (C-D) Bar graph of expression level of *Oct4* and *Nanog* in ES and XEN cells under
691 maintenance conditions. *Rpl14* was used a constitutive gene for qRT-PCR. (n = three
692 biological replicates, $^{***}P$ <0.001).
693 (E-H) Bar graph of expression level of *Gata6*, *Sox7*, *Dab2*, and *Foxa2* in ES and XEN
694 cells under maintenance conditions. *Rpl14* was used a constitutive gene for qRT-PCR. (n
695 = three biological replicates, $^{*}P$ <0.05, $^{**}P$ <0.01).

696 **Figure S2. GO term analysis of ES and XEN cells.**

697 (A-B) Bar graph representing top 10 enriched GO biological processes terms in ES cells
698 from transcriptomic and proteomic dataset.

699 (C-D) Bar graph representing top 10 enriched GO biological processes terms in XEN cells
700 from transcriptomic and proteomic dataset.

701 (E-F) Bar graph representing top 10 enriched GO cellular compartments terms in ES cells
702 from transcriptomic and proteomic dataset.

703 (G-H) Bar graph representing top 10 enriched GO cellular compartments terms in XEN
704 cells from transcriptomic and proteomic dataset.

705 (I-J) Bar graph representing top 10 enriched GO molecular functions terms in ES cells
706 from transcriptomic and proteomic dataset.

707 (K-L) Bar graph representing top 10 enriched GO molecular functions terms in XEN cells
708 from transcriptomic and proteomic dataset.

709 **Figure S3. *In vitro* induction of ES cells towards the XEN lineage.**

710 (A) Schematic diagram of the methodology of cXEN induction *in* vitro.

711 (B-C) Bar graph of expression level of *Nanog* and *Oct4* in ES cells induced towards the
712 XEN lineage over 8 days. *Rpl14* was used a constitutive gene for qRT-PCR. (n = three
713 biological replicates).

714 (D-E) Bar graph of expression level of *Gata6* and *Dab2* in ES cells induced towards the
715 XEN lineage over 8 days. *Rpl14* was used a constitutive gene for qRT-PCR. (n = three
716 biological replicates).

Figure 1

A

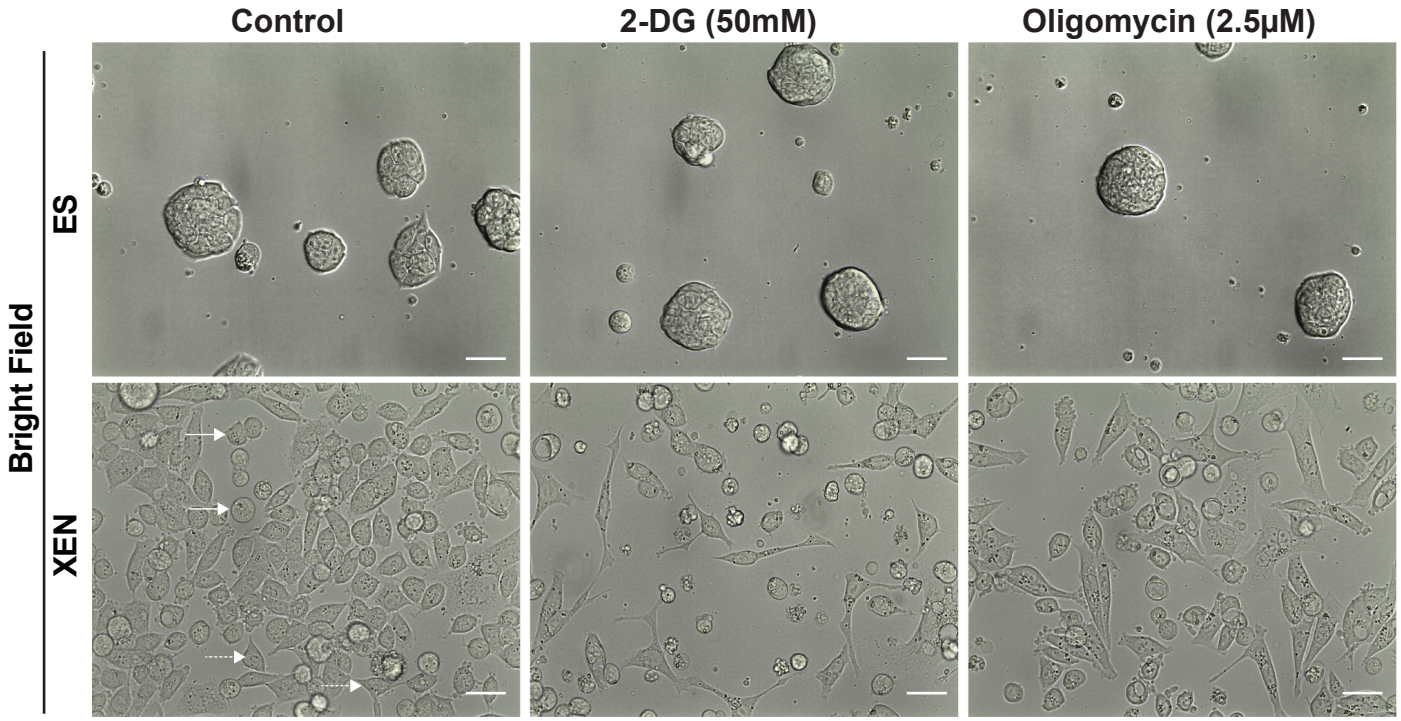
Control
2-DG (50mM)
Oligomycin (2.5μM)
Bright Field
ES
XEN

B

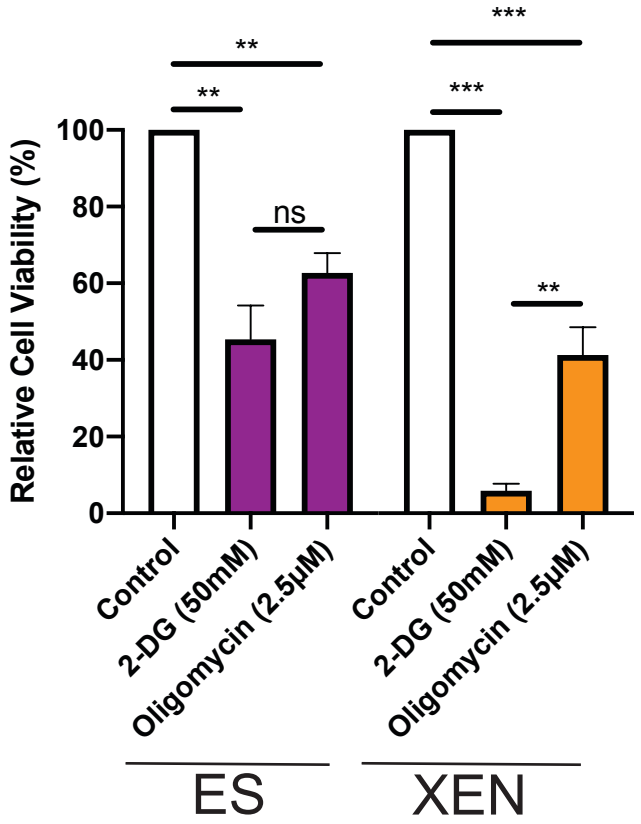
Relative Cell Viability (%)
100
80
60
40
20
0
**
**
ns
***
***
**
Control
2-DG (50mM)
Oligomycin (2.5μM)
Control
2-DG (50mM)
Oligomycin (2.5μM)
ES
XEN

C

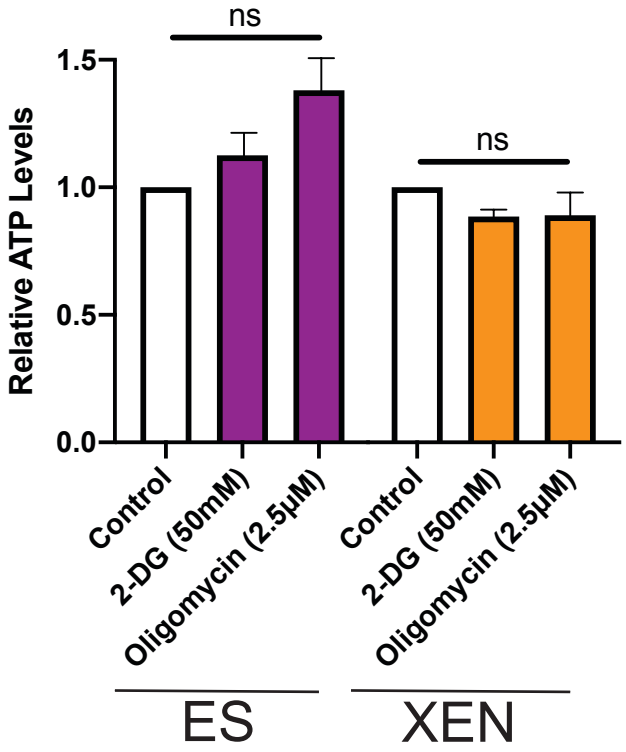
Relative ATP Levels
1.5
1.0
0.5
0.0
ns
ns
Control
2-DG (50mM)
Oligomycin (2.5μM)
Control
2-DG (50mM)
Oligomycin (2.5μM)
ES
XEN

Figure 2

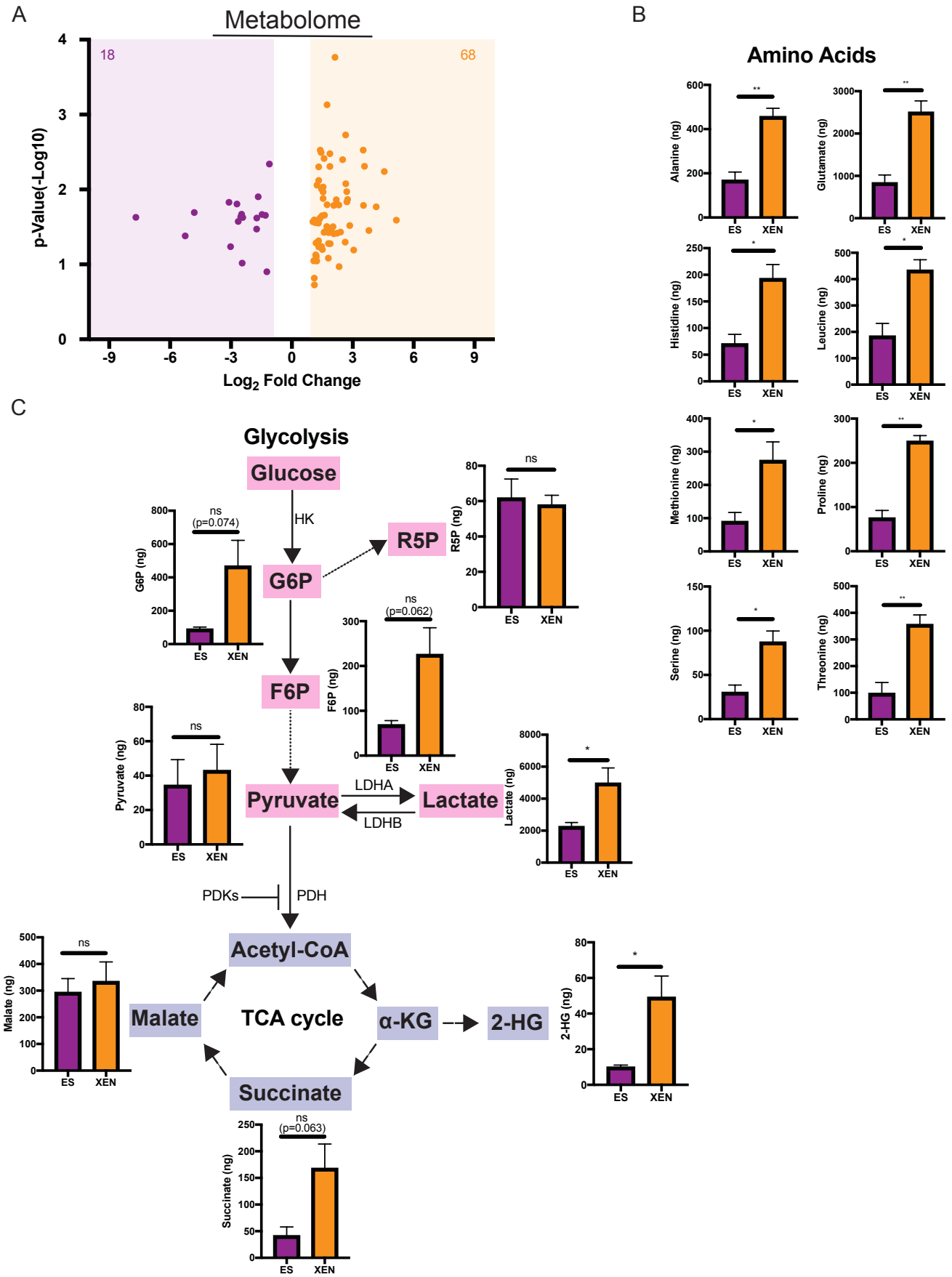
A
Metabolome
18
68
p-Value(-Log10)
Log2 Fold Change
B
Amino Acids
Alanine (ng)
Glutamate (ng)
Histidine (ng)
Leucine (ng)
Methionine (ng)
Proline (ng)
Serine (ng)
Threonine (ng)
ES
XEN
C
Glycolysis
Glucose
HK
G6P
R5P
F6P
Pyruvate
LDHA
LDHB
Lactate
PDKs
PDH
Acetyl-CoA
TCA cycle
Malate
α-KG
2-HG
Succinate
G6P (ng)
R5P (ng)
F6P (ng)
Pyruvate (ng)
Lactate (ng)
Malate (ng)
2-HG (ng)
Succinate (ng)
ns
(p=0.074)
(p=0.062)
(p=0.063)

Figure 3

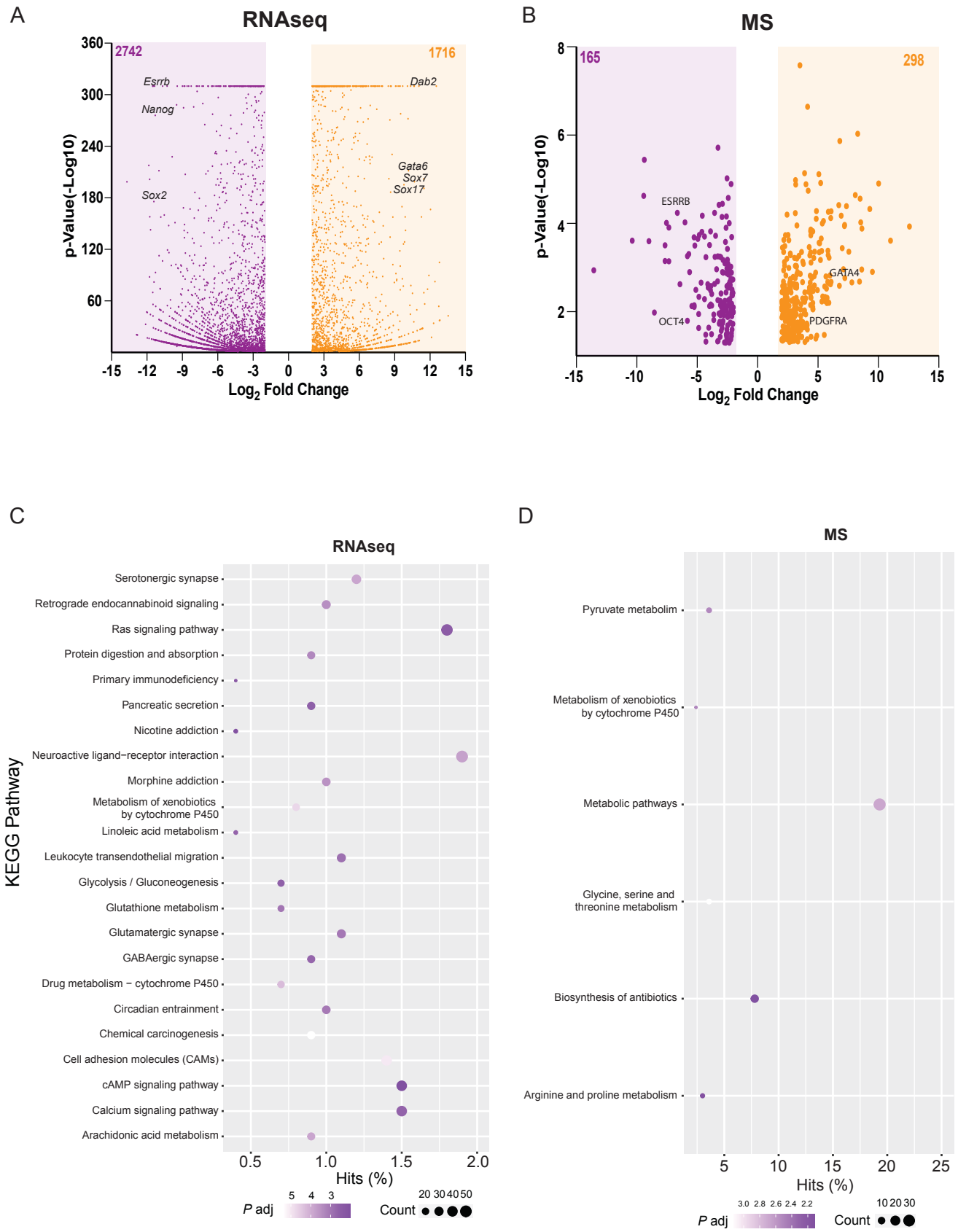
A
RNAseq
2742
1716
Esrrb
Nanog
Sox2
Dab2
Gata6
Sox7
Sox17
p-Value(-Log10)
Log2 Fold Change
B
MS
165
298
ESRRB
OCT4
GATA4
PDGFRA
p-Value(-Log10)
Log2 Fold Change
C
RNAseq
KEGG Pathway
Serotonergic synapse
Retrograde endocannabinoid signaling
Ras signaling pathway
Protein digestion and absorption
Primary immunodeficiency
Pancreatic secretion
Nicotine addiction
Neuroactive ligand−receptor interaction
Morphine addiction
Metabolism of xenobiotics by cytochrome P450
Linoleic acid metabolism
Leukocyte transendothelial migration
Glycolysis / Gluconeogenesis
Glutathione metabolism
Glutamatergic synapse
GABAergic synapse
Drug metabolism − cytochrome P450
Circadian entrainment
Chemical carcinogenesis
Cell adhesion molecules (CAMs)
cAMP signaling pathway
Calcium signaling pathway
Arachidonic acid metabolism
Hits (%)
P adj
Count
D
MS
Pyruvate metabolim
Metabolism of xenobiotics by cytochrome P450
Metabolic pathways
Glycine, serine and threonine metabolism
Biosynthesis of antibiotics
Arginine and proline metabolism
Hits (%)
P adj
Count

Figure 3 cont.

E

F

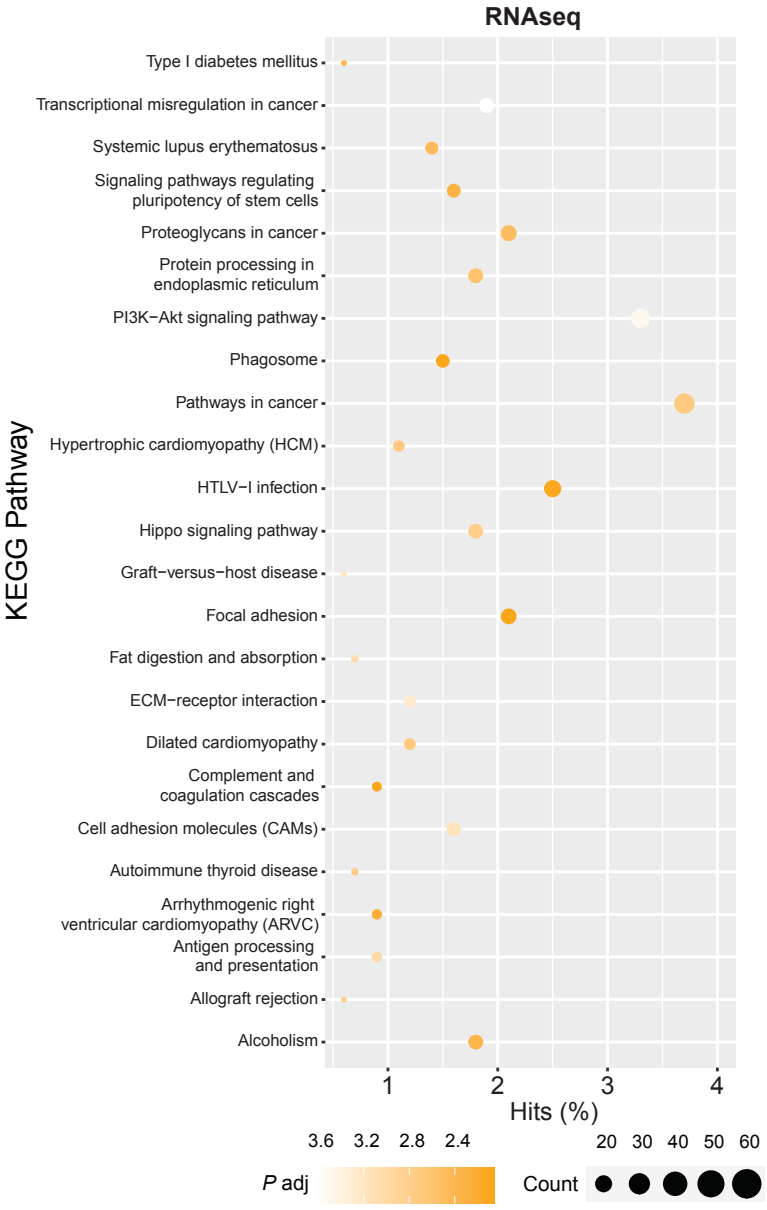

G

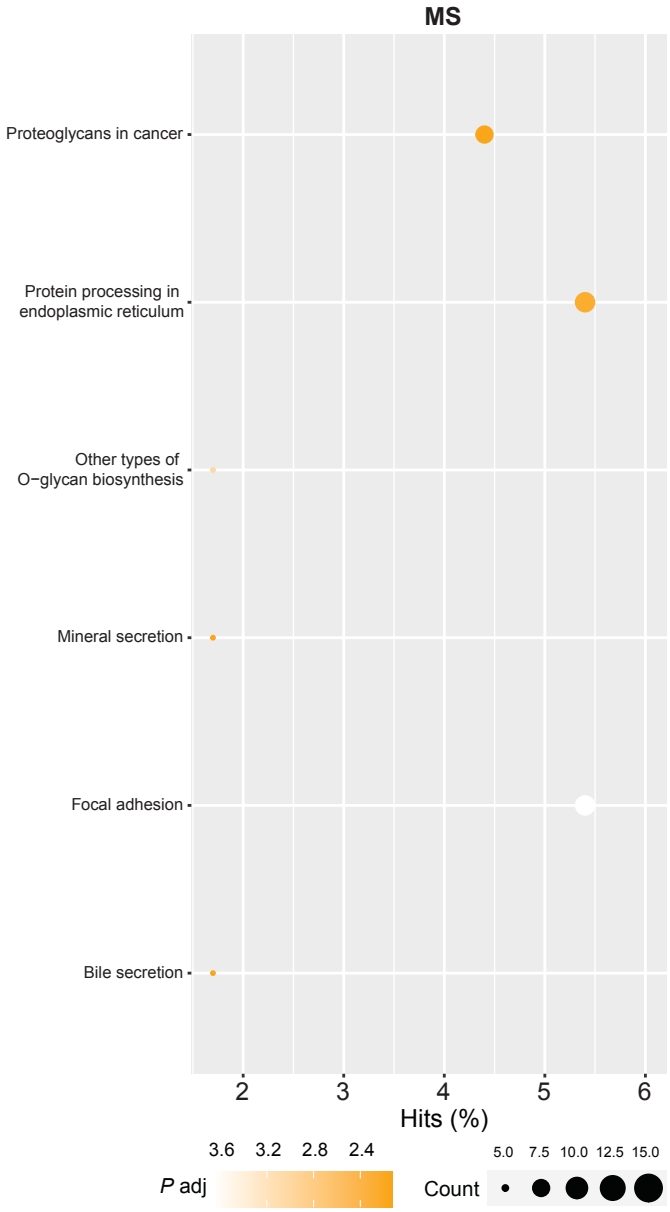

Figure 4

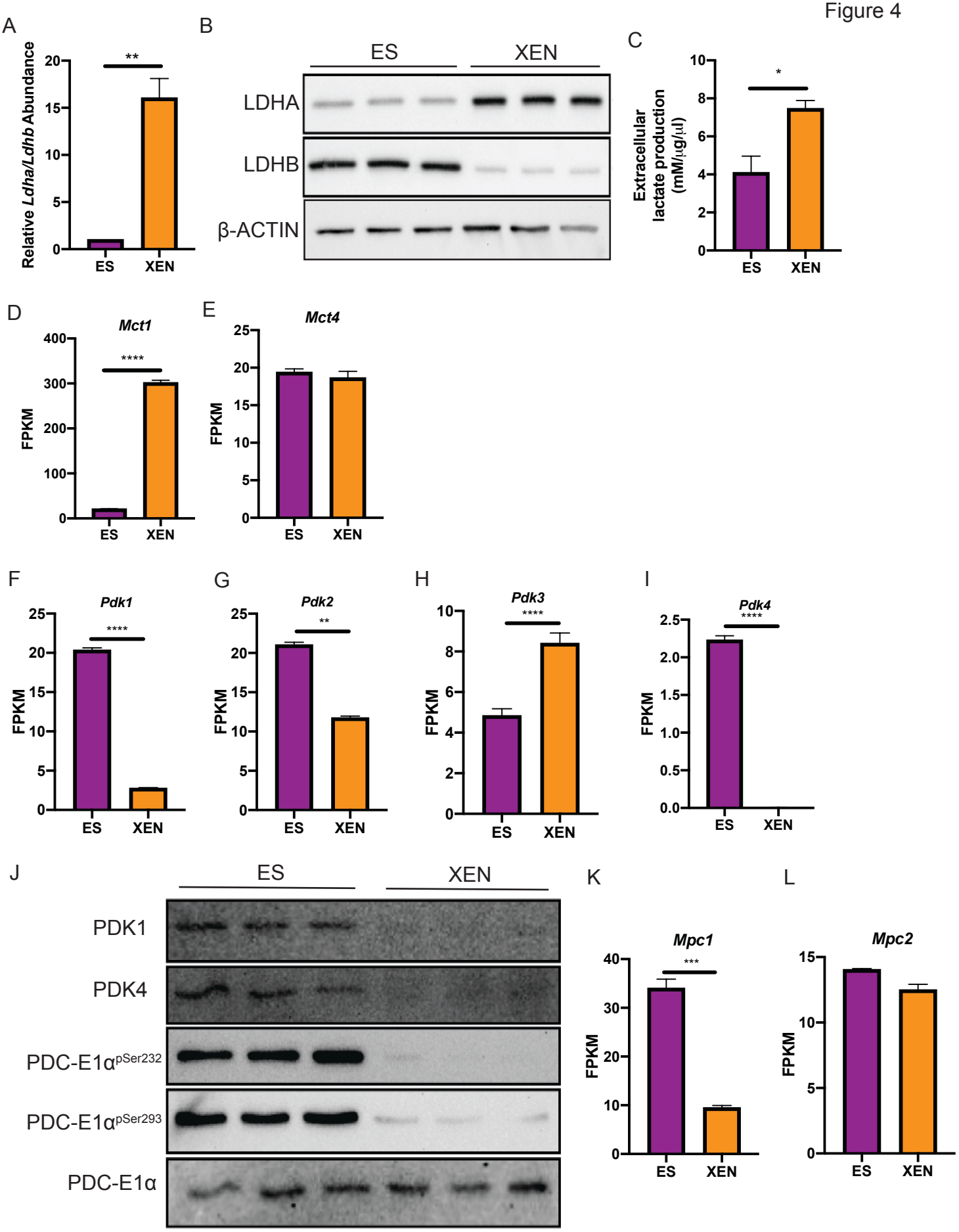
A
Relative Ldha/Ldhb Abundance
20
15
10
5
0
**
ES
XEN
B
ES
XEN
LDHA
LDHB
β-ACTIN
C
Extracellular lactate production (mM/μg/μl)
10
8
6
4
2
0
*
ES
XEN
D
Mct1
FPKM
400
300
200
100
0
****
ES
XEN
E
Mct4
FPKM
25
20
15
10
5
0
ES
XEN
F
Pdk1
FPKM
25
20
15
10
5
0
****
ES
XEN
G
Pdk2
FPKM
25
20
15
10
5
0
**
ES
XEN
H
Pdk3
FPKM
10
8
6
4
2
0
****
ES
XEN
I
Pdk4
FPKM
2.5
2.0
1.5
1.0
0.5
0.0
****
ES
XEN
J
ES
XEN
PDK1
PDK4
PDC-E1α pSer232
PDC-E1α pSer293
PDC-E1α
K
Mpc1
FPKM
40
30
20
10
0
***
ES
XEN
L
Mpc2
FPKM
15
10
5
0
ES
XEN

Figure 5

A

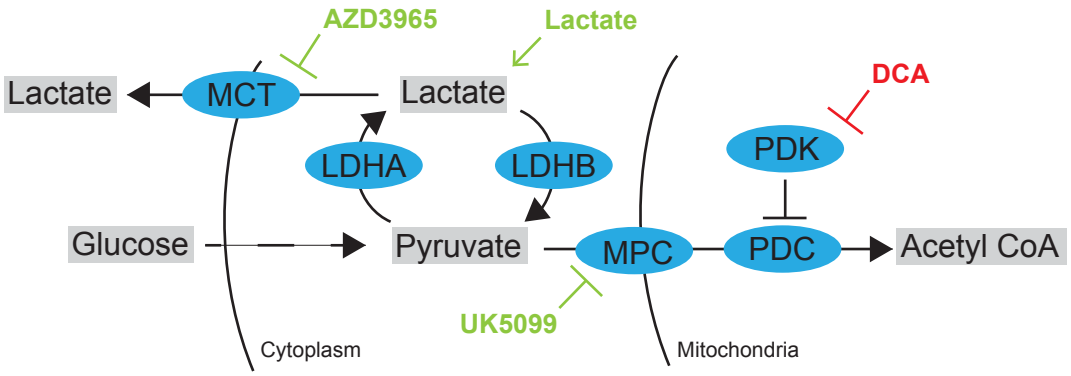

B

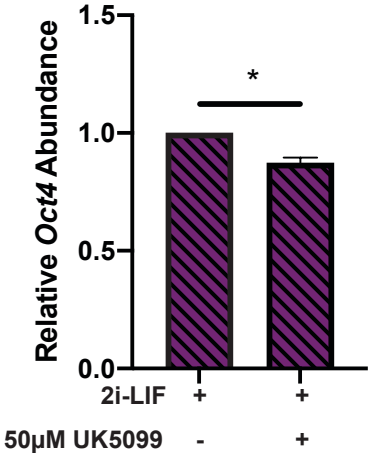

C

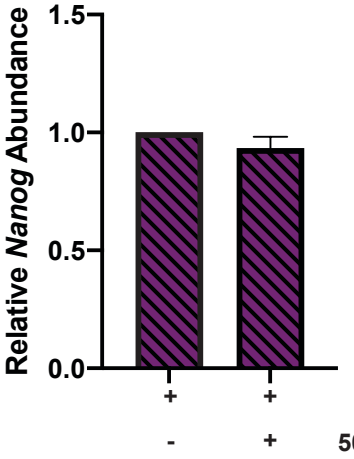

D

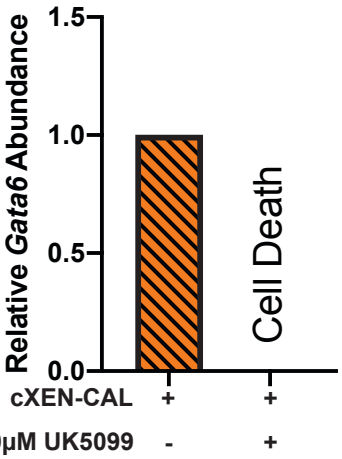

E

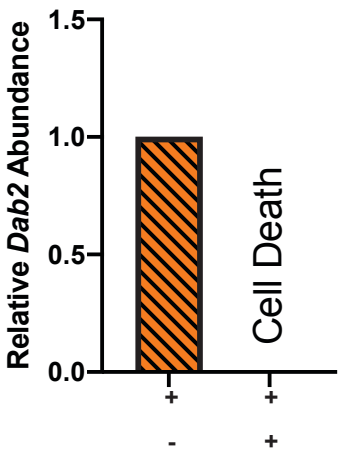

F

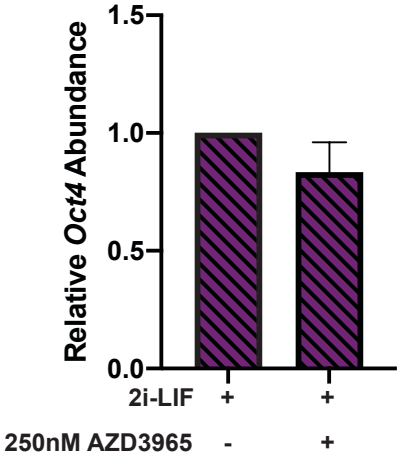

G

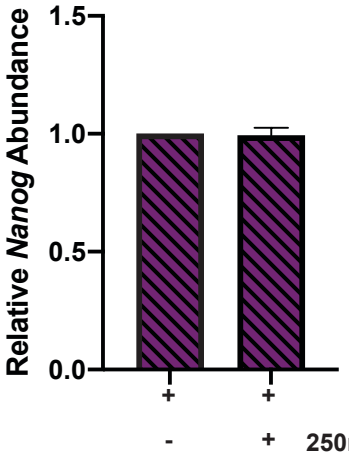

H

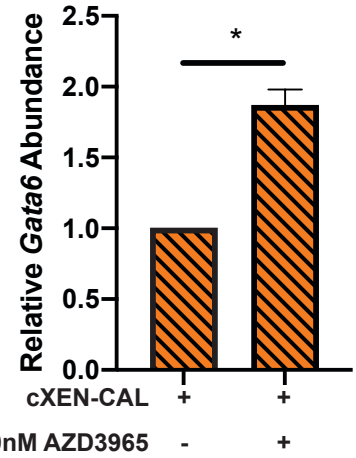

I

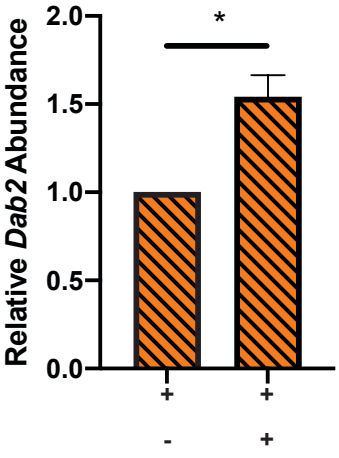

Figure 5 cont.

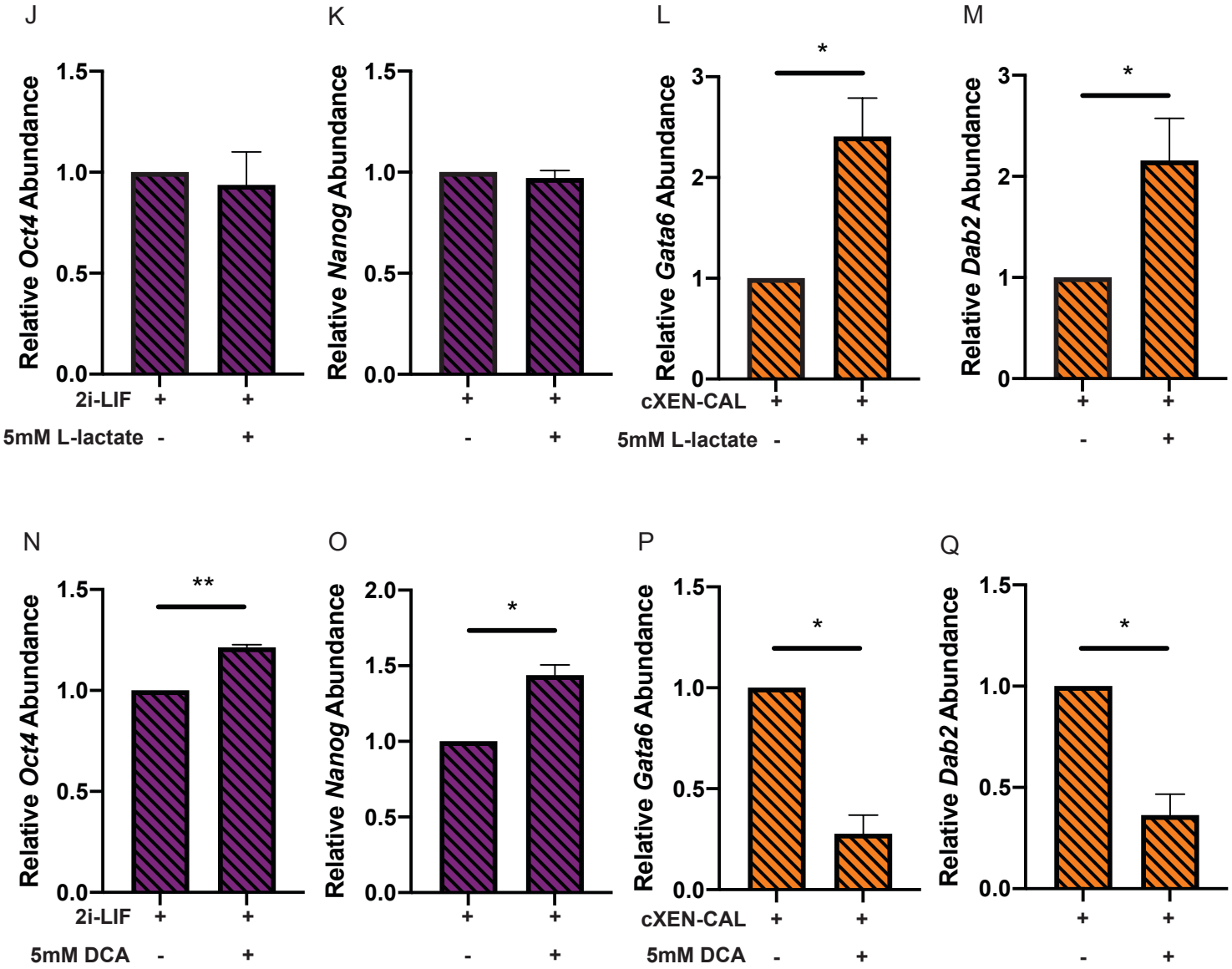

Figure S1

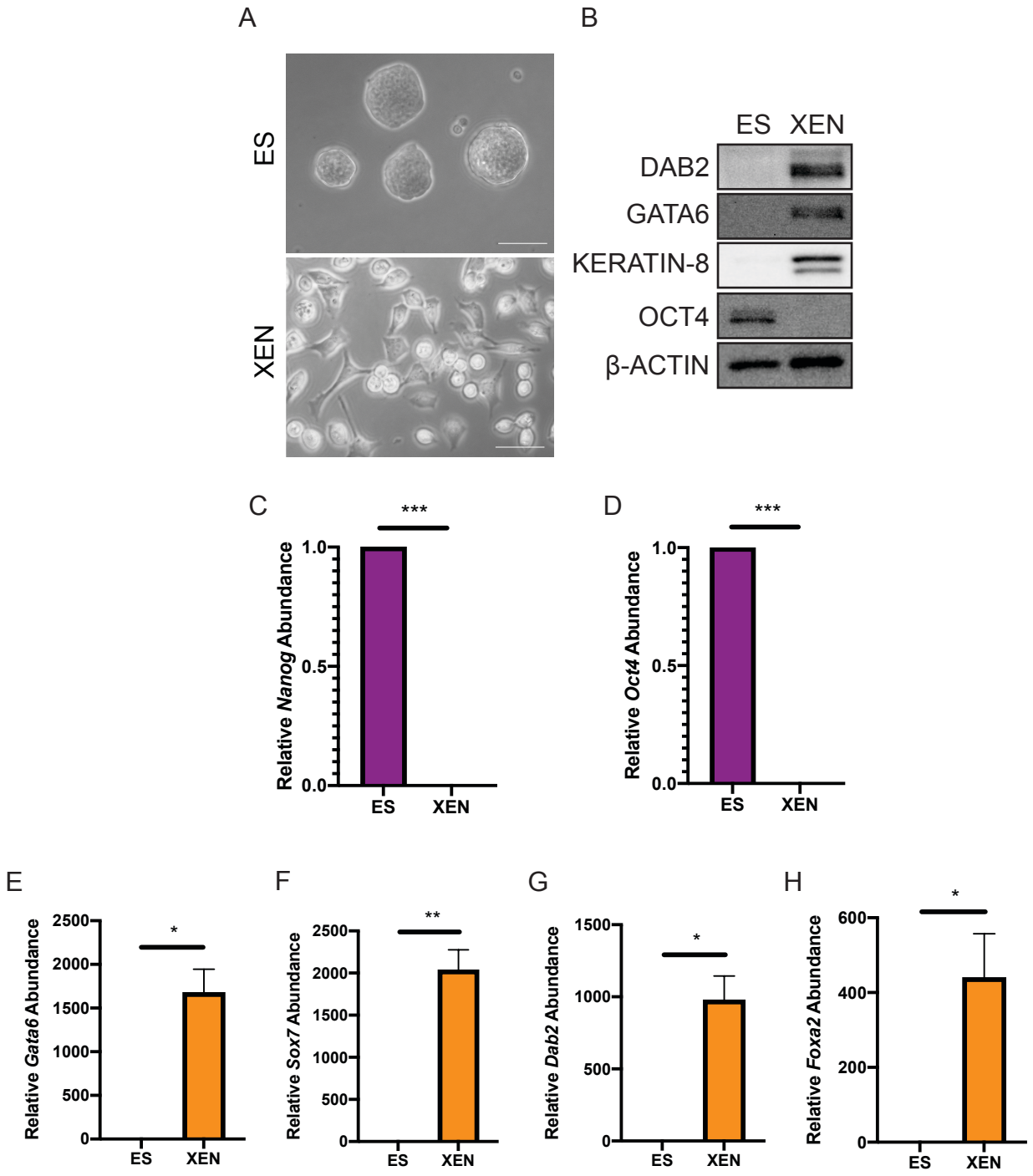
A
ES
XEN
B
ES XEN
DAB2
GATA6
KERATIN-8
OCT4
β-ACTIN
C
***
Relative Nanog Abundance
1.0
0.5
0.0
ES
XEN
D
***
Relative Oct4 Abundance
1.0
0.5
0.0
ES
XEN
E
*
Relative Gata6 Abundance
2500
2000
1500
1000
500
0
ES
XEN
F
**
Relative Sox7 Abundance
2500
2000
1500
1000
500
0
ES
XEN
G
*
Relative Dab2 Abundance
1500
1000
500
0
ES
XEN
H
*
Relative Foxa2 Abundance
600
400
200
0
ES
XEN

Figure S2

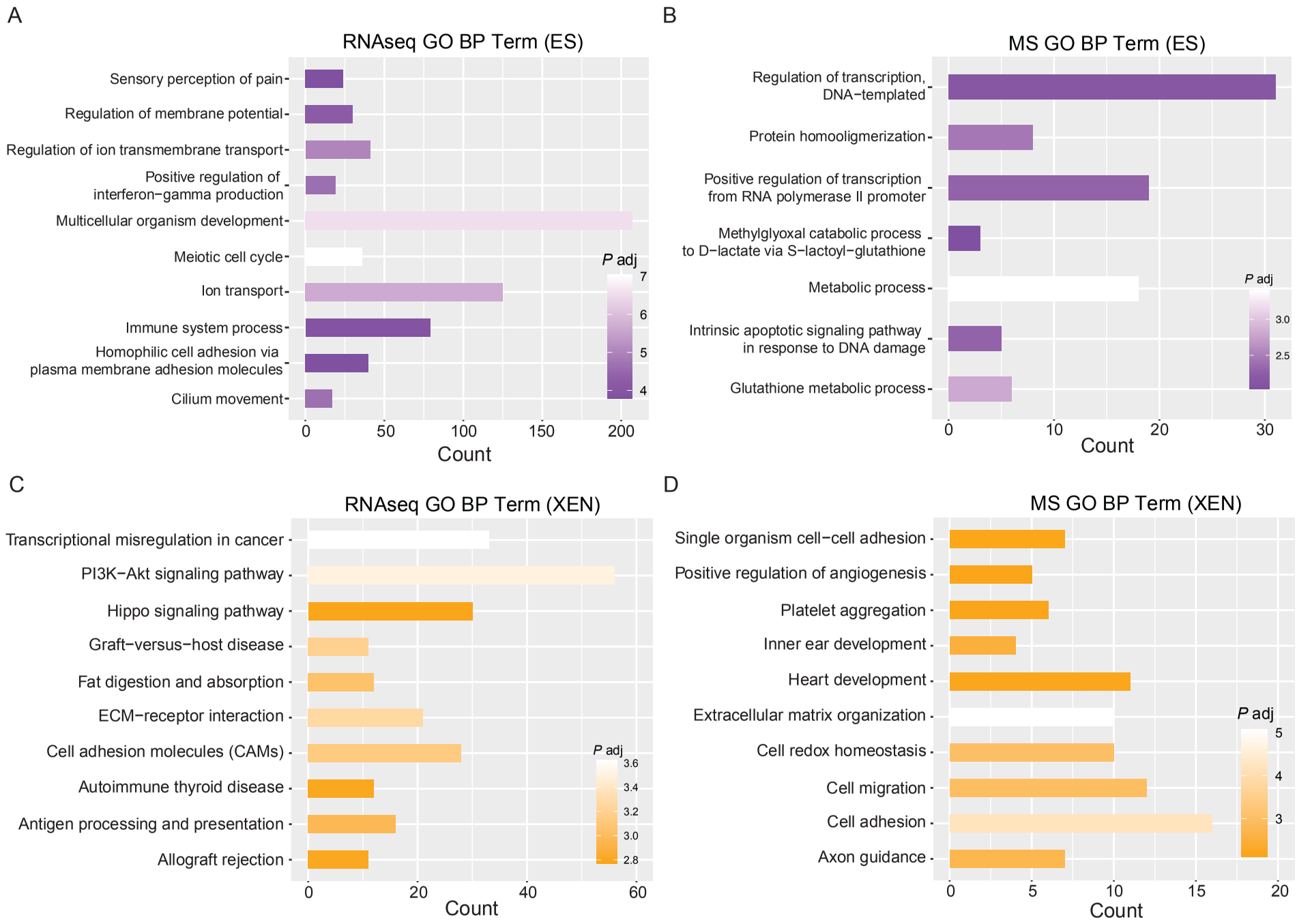
A
RNAseq GO BP Term (ES)
Sensory perception of pain
Regulation of membrane potential
Regulation of ion transmembrane transport
Positive regulation of interferon−gamma production
Multicellular organism development
Meiotic cell cycle
Ion transport
Immune system process
Homophilic cell adhesion via plasma membrane adhesion molecules
Cilium movement
0
50
100
150
200
Count
P adj
7
6
5
4
B
MS GO BP Term (ES)
Regulation of transcription, DNA−templated
Protein homooligmerization
Positive regulation of transcription from RNA polymerase II promoter
Methylglyoxal catabolic process to D−lactate via S−lactoyl−glutathione
Metabolic process
Intrinsic apoptotic signaling pathway in response to DNA damage
Glutathione metabolic process
0
10
20
30
Count
P adj
3.0
2.5
C
RNAseq GO BP Term (XEN)
Transcriptional misregulation in cancer
PI3K−Akt signaling pathway
Hippo signaling pathway
Graft−versus−host disease
Fat digestion and absorption
ECM−receptor interaction
Cell adhesion molecules (CAMs)
Autoimmune thyroid disease
Antigen processing and presentation
Allograft rejection
0
20
40
60
Count
P adj
3.6
3.4
3.2
3.0
2.8
D
MS GO BP Term (XEN)
Single organism cell−cell adhesion
Positive regulation of angiogenesis
Platelet aggregation
Inner ear development
Heart development
Extracellular matrix organization
Cell redox homeostasis
Cell migration
Cell adhesion
Axon guidance
0
5
10
15
20
Count
P adj
5
4
3

Figure S2

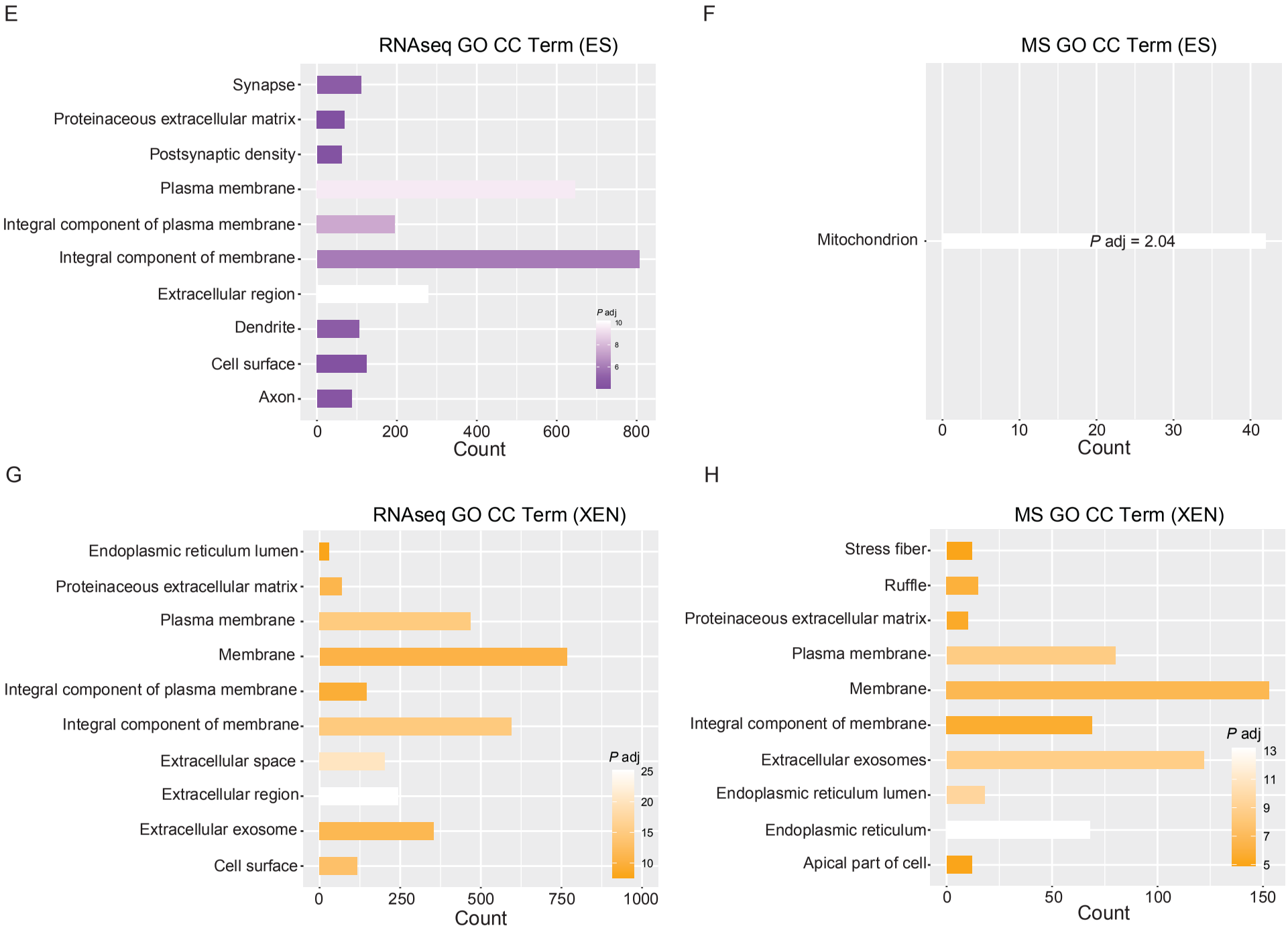
E
RNAseq GO CC Term (ES)
Synapse
Proteinaceous extracellular matrix
Postsynaptic density
Plasma membrane
Integral component of plasma membrane
Integral component of membrane
Extracellular region
Dendrite
Cell surface
Axon
P adj
10
8
6
0
200
400
600
800
Count
F
MS GO CC Term (ES)
Mitochondrion
P adj = 2.04
0
10
20
30
40
Count
G
RNAseq GO CC Term (XEN)
Endoplasmic reticulum lumen
Proteinaceous extracellular matrix
Plasma membrane
Membrane
Integral component of plasma membrane
Integral component of membrane
Extracellular space
Extracellular region
Extracellular exosome
Cell surface
P adj
25
20
15
10
0
250
500
750
1000
Count
H
MS GO CC Term (XEN)
Stress fiber
Ruffle
Proteinaceous extracellular matrix
Plasma membrane
Membrane
Integral component of membrane
Extracellular exosomes
Endoplasmic reticulum lumen
Endoplasmic reticulum
Apical part of cell
P adj
13
11
9
7
5
0
50
100
150
Count

Figure S2

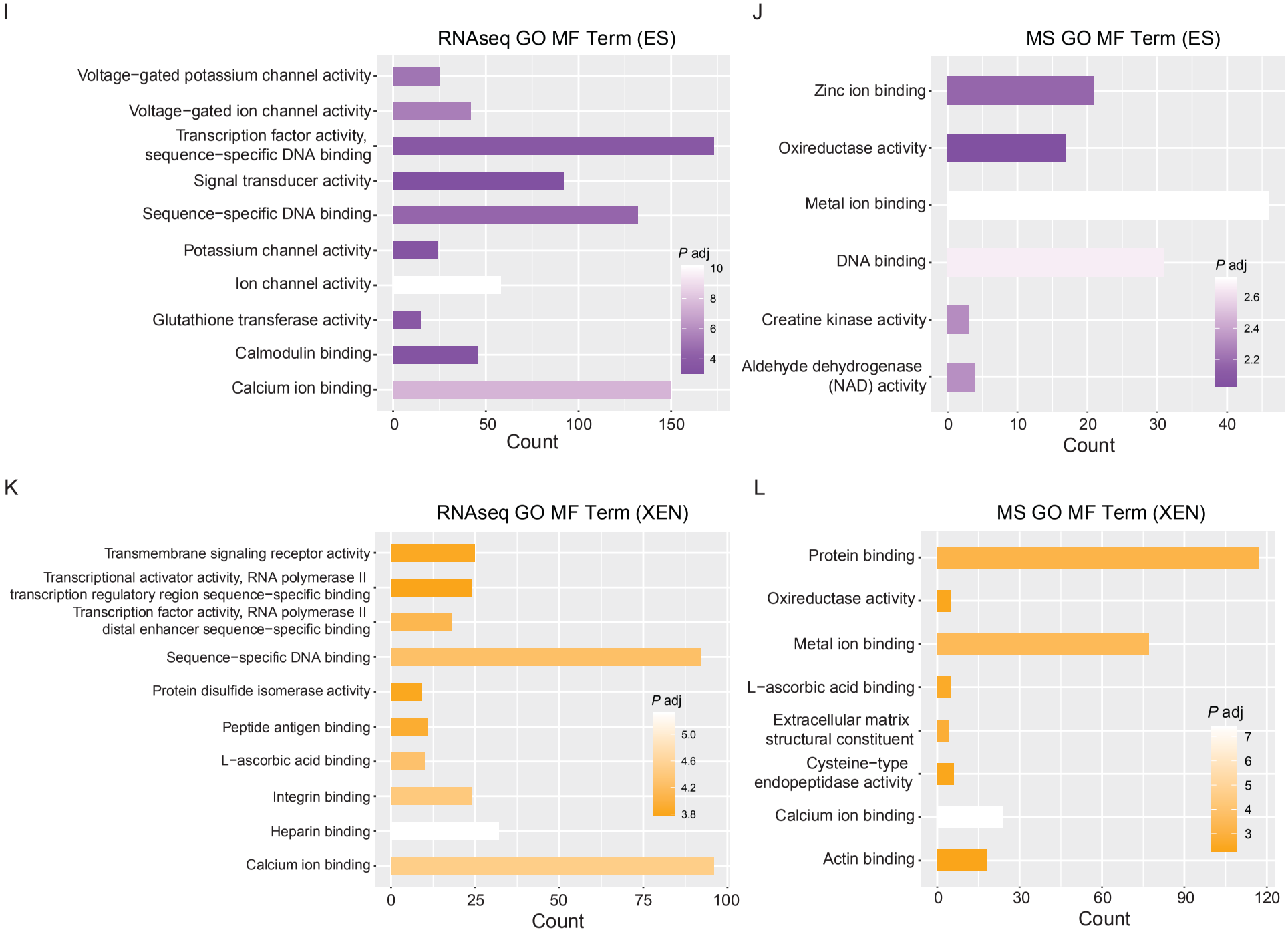
I
RNAseq GO MF Term (ES)
Voltage−gated potassium channel activity
Voltage−gated ion channel activity
Transcription factor activity, sequence−specific DNA binding
Signal transducer activity
Sequence−specific DNA binding
Potassium channel activity
Ion channel activity
Glutathione transferase activity
Calmodulin binding
Calcium ion binding
P adj
10
8
6
4
0
50
100
150
Count
J
MS GO MF Term (ES)
Zinc ion binding
Oxireductase activity
Metal ion binding
DNA binding
Creatine kinase activity
Aldehyde dehydrogenase (NAD) activity
P adj
2.6
2.4
2.2
0
10
20
30
40
Count
K
RNAseq GO MF Term (XEN)
Transmembrane signaling receptor activity
Transcriptional activator activity, RNA polymerase II transcription regulatory region sequence−specific binding
Transcription factor activity, RNA polymerase II distal enhancer sequence−specific binding
Sequence−specific DNA binding
Protein disulfide isomerase activity
Peptide antigen binding
L−ascorbic acid binding
Integrin binding
Heparin binding
Calcium ion binding
P adj
5.0
4.6
4.2
3.8
0
25
50
75
100
Count
L
MS GO MF Term (XEN)
Protein binding
Oxireductase activity
Metal ion binding
L−ascorbic acid binding
Extracellular matrix structural constituent
Cysteine−type endopeptidase activity
Calcium ion binding
Actin binding
P adj
7
6
5
4
3
0
30
60
90
120
Count

Figure S3

A

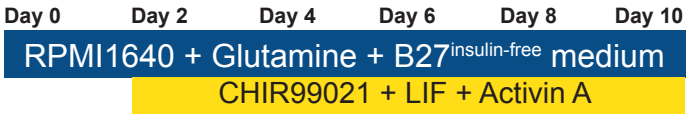

B

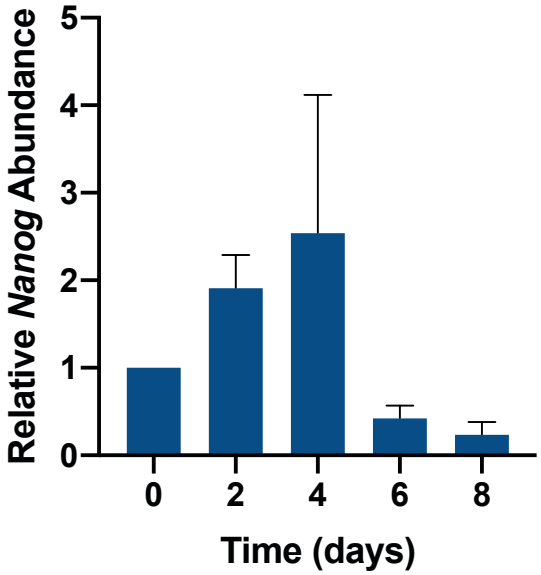

C

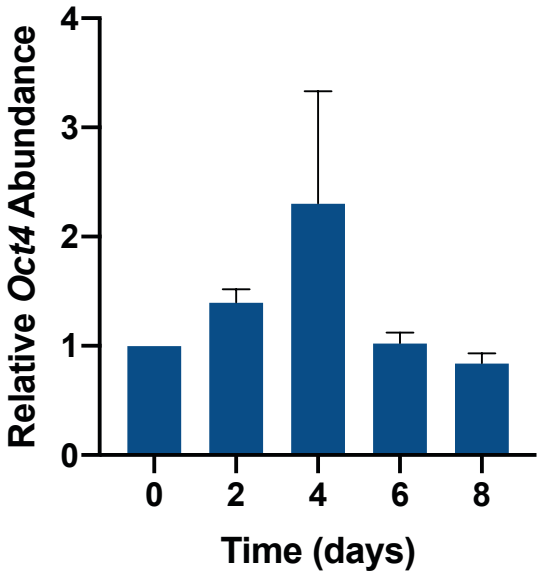

D

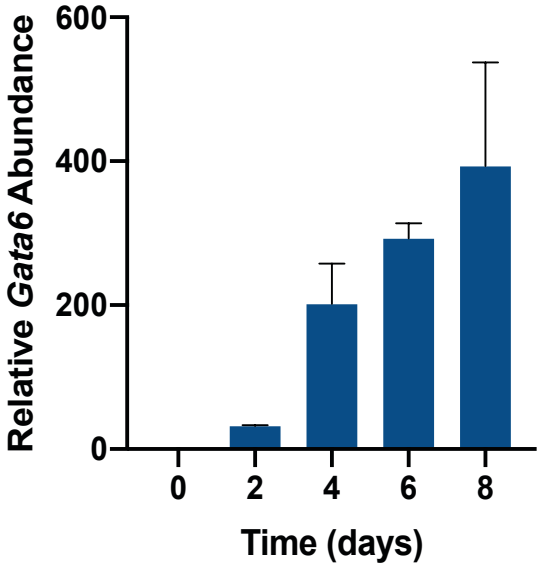

E

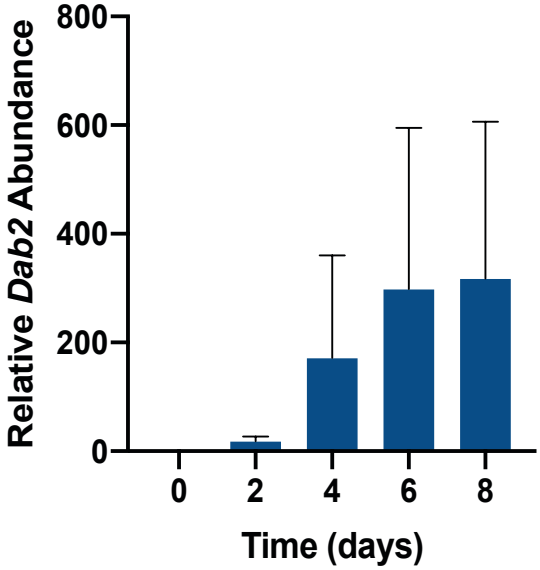

Tables:

Table 1. Metabolites enriched in either ES or XEN cells based on untargeted/targeted metabolomics

ES	XEN
Choline	Indole
Dimethylglycine	Betaine
N-acetylputrescine	Purine
Cytidine	Methylcysteine
Acadesine	2-Aminooctanoic acid
Adenosine	Methionine sulfoxide
Guanosine	N-carbamoyl-L-aspartate
Aminoimidazole carboxamide ribonucleotide	N-acetyl-glutamine
Glycerate	N-acetyl-glutamate
Carbamoyl phosphate	Ng,NG-dimethyl-L-arginine
Glucono-D-lactone	N-acetyl-glucosamine
2-dehydro-D-gluconate	Carnosine
Uridine	Glycerophosphocholine
Inosine	1-Methyladenosine
Sedoheptulose-1,7-bisphosphate	dCMP
Dihydroxy-acetone-phosphate	dAMP
Ethanolamine	GMP
Acylcarnitine C6:0	S-adenosyl-L-methionine
	Glutathione disulfide
	Methylmalonic acid
	N-acetyl-L-alanine
	Orotate
	Allantoin
	Phenylpyruvate
	Phenyllactic acid
	Uric acid
	sn-glycerol-3-phosphate
	Myo-inositol
	Xanthurenic acid
	Deoxyribose-phosphate
	2,3-diphosphoglyceric acid
	Glutathione
	UDP-D-glucose
	UDP-N-acetyl-glucosamine
	Taurine
	a-ketoglutarate
	Phosphoenolpyruvate
	AMP
	Hydroxyproline
	Asparagine

	Kynurenine
	Sarcosine
	Acylcarnitine C2:0
	Acylcarnitine C3:0
	Acylcarnitine C4:0
	Acylcarnitine C5:0
	Acylcarnitine C14:0
	Acylcarnitine C16:0
	Acylcarnitine C16-OH
	Acylcarnitine C18:0
	Lactate
	Succinate
	2-hydroxygluterate
	Glucose-6-phosphate
	Fructose-6-phophate
	Alanine
	4-aminobutyrate
	Serine
	Proline
	Threonine
	Leucine
	Glutamate
	Methionine
	Histidine
	Arginine
	Citrulline
	Tyrosine
	Tryptophan

Table 2. Products, manufacturer and catalogue number of items used in this report

Product	Source	Catalogue number
Neurobasal™ medium	Thermo Fisher Scientific	21103049
KnockOut™ DMEM/F-12	Thermo Fisher Scientific	12660012
N-2	Thermo Fisher Scientific	17502001
B-27™ (minus vitamin A)	Thermo Fisher Scientific	12587010
B-27™ (minus insulin)	Thermo Fisher Scientific	A1895601
GlutaMAX™	Thermo Fisher Scientific	35050061
2-mercaptoethanol	Thermo Fisher Scientific	31350010
StemPro™ Accutase™	Thermo Fisher Scientific	A1110501
RPMI 1640 medium	Thermo Fisher Scientific	42401018
Fetal bovine serum	Thermo Fisher Scientific	12484028
TrypLE™ Express	Thermo Fisher Scientific	12605010
Gelatin	BDH	B44045
ESGRO™ recombinant mouse LIF protein	Millipore-Sigma	ESG1106
CHIR-99021	APExBIO	A3011
PD0325901	APExBIO	A3013
Recombinant Human/Mouse/Rat Activin A protein	R&D Systems	338-AC-050
QIAshredder	Qiagen	79654
RNeasy mini kit	Qiagen	74104
High-capacity cDNA reverse transcription kit	Thermo Fisher Scientific	4368814
SensiFAST Sybr No-ROX	FroggaBio	BIO-98050
HALT™ protease inhibitor cocktail	Thermo Fisher Scientific	78425
DC protein assay	Bio-Rad	5000111
Immuno-Blot PVDF membrane	Bio-Rad	1620177
Pierce™ 600nm protein assay kit	Thermo Fisher Scientific	22662
CellTiter-Glo® luminescent cell viability assay	Promega	G7570
2-deoxy-D-glucose	BioShop Canada Inc.	DXG498
Oligomycin A	Millipore-Sigma	75351
UK5099	Cayman Chemicals	16980
AZD3965	Cayman Chemicals	19912
Sodium dichloroacetate	Millipore-Sigma	347795
Sodium L-lactate	Millipore-Sigma	L7002

Table 3. Primary and secondary antibodies used in this report

Antibody	Source	Catalogue number
Mouse monoclonal to PDK1	Santa Cruz	sc-293160
Mouse monoclonal to PDK4	Santa Cruz	sc-28783
Rabbit polyclonal to PDC-E1α^{pSer232}	Millipore-Sigma	AP1063
Rabbit polyclonal to PDC-E1α^{pSer293}	Novus Biologicals	NB110-93479
Mouse monoclonal to PDC-E1α	Abcam	Ab110334
Rabbit monoclonal to LDHA	Cell Signalling Technology	3582
Mouse monoclonal to LDHB	Abcam	Ab85319
Mouse monoclonal to β-ACTIN	Santa Cruz	sc-69879
Rabbit polyclonal to DAB2	Cell Signalling Technology	12906S
Goat polyclonal to GATA6	Novus Biologicals	AF1700
Rat monoclonal to KERATIN-8	DSHB	TROMA-I-f
Rabbit polyclonal to OCT4	Cell Signalling Technology	2750
Goat anti-rabbit IgG-HRP	Millipore-Sigma	AQ132P
Goat anti-mouse IgG-HRP	Millipore-Sigma	A5278
Goat anti-rat IgG-HRP	Abcam	Ab97057
Rabbit anti-goat IgG-GRP	Millipore-Sigma	A8919

Table 4. Primer sequences used in this report

Gene name	Forward sequence	Reverse sequence
Ldha	TGG CGA CTC CAG TGT GCC TG	AGG CAC TGT CCA CCA CCT GCT
Ldhb	GGG AAA GTC TCT GGC TGA TGAA	CTG TCA CAG AGT AAT CTT TAT CGG C
Oct4	CCC AAT GCC GTG AAG TTG GA	GCT TTC ATG TCC TGG GAC TCC T
Nanog	TCT TCC TGG TCC CCA CAG TTT	GCA AGA ATA GTT CTC GGG ATG AA
Gata6	ATG GCG TAG AAA TGC TGA GG	TGA GGT GGT CGC TTG TGT AG
Dab2	GGA GCA TGT AGA CCA TGA TG	AAA GGA TTT CCG AAA GGG CT
Foxa2	CCC TAC GCC AAC ATG AAC TCG	GTT CTG CCG GTA GAA AGG GA
Rpl14	GGG TGG CCT ACA TTT CCT TCG	GAG TAC AGG GTC CAT CCA CTA AA